Research Square

Preprints are preliminary reports that have not undergone peer review.
They should not be considered conclusive, used to inform clinical practice,
or referenced by the media as validated information.

Adipocyte GDI2 suppresses lipophagy to restrain adaptive thermogenesis and promotes diet-induced obesity

Fei Gao
The First Affiliated Hospital of Shandong First Medical University & Shandong Provincial Qianfoshan Hospital

Yongjiao Zhang
The First Affiliated Hospital of Shandong First Medical University & Shandong Provincial Qianfoshan Hospital

Dong Liu
The First Affiliated Hospital of Shandong First Medical University & Shandong Provincial Qianfoshan Hospital

Yufan Song
The First Affiliated Hospital of Shandong First Medical University & Shandong Provincial Qianfoshan Hospital

Yang Sun
The First Affiliated Hospital of Shandong First Medical University & Shandong Provincial Qianfoshan Hospital

Meitian Wang
wmt0409@163.com

Qilu Hospital, Cheeloo College of Medicine, Shandong University

Sumei Lu
The First Affiliated Hospital of Shandong First Medical University & Shandong Provincial Qianfoshan Hospital

Guangyong Zhang
The First Affiliated Hospital of Shandong First Medical University & Shandong Provincial Qianfoshan Hospital

---

Research Article

Keywords: Obesity, white adipose tissue browning, adaptive thermogenesis, GDI2, lipophagy

Posted Date: July 6th, 2026

DOI: https://doi.org/10.21203/rs.3.rs-10151545/v1

License: This work is licensed under a Creative Commons Attribution 4.0 International License.
Read Full License

Additional Declarations: No competing interests reported.

Adipocyte GDI2 suppresses lipophagy to restrain adaptive thermogenesis and promotes diet-induced obesity

Fei Gao[1], Yongjiao Zhang[1], Dong Liu[1], Yufan Song[1], Yang Sun[1], Meitian Wang[4,5*], Sumei Lu[1*], Guangyong Zhang[2,3*]

[1]Department of Clinical Laboratory Medicine, The First Affiliated Hospital of Shandong First Medical University & Shandong Provincial Qianfoshan Hospital, Jinan, Shandong, 250014, China.

[2]Department of General Surgery, The First Affiliated Hospital of Shandong First Medical University & Shandong Provincial Qianfoshan Hospital, Jinan, Shandong, 250014, China.

[3]Laboratory of Metabolism and Gastrointestinal Tumor, The First Affiliated Hospital of Shandong First Medical University & Shandong Provincial Qianfoshan Hospital, Jinan, China

[4]Department of Clinical Laboratory, Qilu Hospital, Cheeloo College of Medicine, Shandong University, No. 107 Wenhua West Road, Jinan, Shandong, 250012, China.

[5]Department of Clinical Laboratory, Qilu Hospital (Qingdao), Cheeloo College of Medicine, Shandong University, No. 758 Hefei Road, Qingdao, Shandong, 266035, China.

*Corresponding authors: Meitian Wang, Sumei Lu, Guangyong Zhang

E-mail: wmt0409@163.com; lusumei@sdfmu.edu.cn; gyzhang3369@sdfmu.edu.cn

ABSTRACT

Background

Promoting the thermogenic remodeling of white adipose tissue (WAT) is a promising strategy to combat obesity. Lipophagy degrades lipid droplets to supply free fatty acids that fuel thermogenesis in beige adipocytes. GDP dissociation inhibitor 2 (GDI2) is a negative regulator of Rab GTPases implicated in adipocyte lipid storage, but its role in

lipophagy-mediated WAT browning has not been explored. This study aimed to characterize GDI2 as a novel regulator of lipophagy and beige fat thermogenesis.

Methods

The metabolic relevance of GDI2 was profiled in differentiated adipocytes, obese mouse models, thermogenic mouse models, and human subjects. Subcellular localization was determined by confocal microscopy and immunogold electron microscopy. Adipocyte-specific *Gdi2* knockout mice were generated and subjected to cold exposure or β3-adrenergic stimulation, and assess thermogenic capacity. Stimulated lipolysis was evaluated in primary adipocytes, *Gdi2*-knockout C3H10T1/2 cells, and *ex vivo* WAT explants. The lipophagy stage at which GDI2 acts was defined by immunoblotting, confocal imaging of lipid droplets with LC3B, autophagic inhibitor treatments, mCherry-EGFP-LC3B reporter, and transmission electron microscopy. RNA-seq was employed to profile downstream transcriptional adaptations. High-fat diet feeding was used to determine whether *Gdi2* deficiency confers resistance to obesity and associated metabolic disorders.

Results

GDI2 expression is positively correlated with BMI in humans and is upregulated in the adipose tissue of obese mice, while it is suppressed by cold exposure. Adipocyte-specific deletion of *Gdi2* in mice promotes cold-induced WAT browning and energy expenditure, and confers resistance to diet-induced obesity, insulin resistance, and hepatic steatosis. Mechanistically, GDI2 acts as a molecular brake on lipophagy by inhibiting the late-stage fusion of autophagosomes with lysosomes independently of the canonical neutral lipolysis pathway. *Gdi2* deficiency releases this brake, accelerating the lipophagic degradation

of lipid droplets and generating a robust supply of free fatty acids. These fatty acids serve as signaling ligands to activate a PPARα/PGC1α-dependent transcriptional program, driving thermogenic and mitochondrial oxidative phosphorylation gene expression to channel lipid flux into energy dissipation.

Conclusions

GDI2 functions as a key inhibitor of adipocyte lipophagy that restrains beige fat thermogenesis, positioning it as a potential therapeutic target to combat obesity and related metabolic disorders.

Key words: Obesity; white adipose tissue browning; adaptive thermogenesis; GDI2; lipophagy

Introduction

Obesity has reached pandemic proportions worldwide, with its prevalence rising rapidly over recent decades and increasingly affecting younger populations [1, 2]. This condition frequently coexists with multiple comorbidities, including type 2 diabetes, metabolic dysfunction-associated steatotic liver disease, and cardiovascular diseases, collectively imposing a substantial burden on public health [3, 4]. Mammalian adipose tissue is classically divided into white adipose tissue (WAT) specialized for energy storage and brown adipose tissue (BAT) responsible for non-shivering thermogenesis [5]. Within WAT resides an inducible beige adipocyte population, which exhibits exceptional metabolic plasticity and robust thermogenic capacity upon cold or β3-adrenergic stimulation [6]. Aberrant expansion and dysfunction of WAT represent the core pathological basis for obesity-induced systemic metabolic imbalance and subsequent multi-organ complications [7]. Promoting WAT

67 browning enhances energy expenditure and improves insulin sensitivity, representing a
68 promising therapeutic target for combating obesity and its associated metabolic disorders.

69 The initiation and maintenance of WAT browning depend on a sustained supply of free
70 fatty acids (FFAs) [8]. FFAs serve not only as substrates for mitochondrial β-oxidation-driven
71 thermogenesis but also as signaling molecules that activate thermogenic gene expression [6,
72 9-11]. Efficient degradation of lipid droplets (LDs) constitutes a prerequisite for FFA release
73 [12, 13]. Intracellular LD degradation is primarily achieved through two complementary
74 pathways: the canonical neutral lipolysis pathway, mediated by neutral lipases such as adipose
75 triglyceride lipase (ATGL) and hormone-sensitive lipase (HSL) for sequential hydrolysis of
76 triglycerides into diacylglycerols and then monoacylglycerol; and the lipophagy pathway, a
77 key form of selective autophagy that engulfs LDs within autophagosomes and subsequently
78 fuses with lysosomes, where lysosomal acid lipase (LAL) degrades the lipid cargo [14-17].
79 Despite the established role of lipophagy in LD degradation, the molecular mechanisms
80 coupling lipophagy to WAT browning and adaptive thermogenesis remain largely unexplored.

81 Rab GTPases, the largest subfamily of small GTPases, serve as central molecular
82 switches that orchestrate intracellular membrane trafficking, organelle crosstalk, and
83 membrane fusion events [18]. Several Rab GTPases have been implicated in lipid metabolism,
84 including LD biogenesis and lipophagy [19-21]. Specifically, Rab7 mediates
85 autophagosome-lysosome fusion and is a key lipophagy effector in hepatocytes and
86 adipocytes; Rab10 facilitates the engulfment and elongation of autophagic membranes around
87 LDs in hepatocellular lipophagy; Rab18 participates in LD growth and maturation, and
88 substate supply for lipophagy [22-27]. Rab protein activity is precisely coordinated by

guanine nucleotide exchange factors (GEFs), GTPase-activating proteins (GAPs), and GDP dissociation inhibitors (GDIs) [28, 29]. For instance, GP73 acts as a GAP for Rab23, contributing to nonalcoholic fatty liver disease, whereas DENND6A serves as a GEF for Rab34 to regulate retrograde lysosomal transport and autophagic flux [30, 31]. Guanine nucleotide dissociation inhibitor 2 (GDI2), a key member of the GDI family, negatively regulates Rab activity by binding to the Rab-GDP proteins, thereby preventing their membrane targeting and activation [32]. Studies have shown that GDI2 participates in the regulation of adipogenic differentiation of preadipocytes [33]. Moreover, GDI2 is upregulated in omental adipose tissue of obese individuals with insulin resistance, where it directly impairs lipid storage by inhibiting insulin-stimulated binding of Rab18 to LD membranes [34]. Nevertheless, the role of GDI2 in WAT browning and adaptive thermogenesis through the regulation of lipid metabolism has not been previously reported.

In this study, we systematically characterized GDI2 as a novel negative regulator of WAT browning and adaptive thermogenesis. Immunogold electron microscopy revealed that GDI2 is localized in the cytosol as well as on membranous structures including LDs, endoplasmic reticulum-LD contact sites, and autophagolysosomal membranes. GDI2 expression levels were positively correlated with body mass index (BMI) in humans, were elevated in adipose tissue of obese mice, and were reduced in adipose tissue of cold-exposed mice, suggesting its involvement in metabolic homeostasis. Using adipocyte-specific *Gdi2* knockout ($Gdi2^{AKO}$) mice, we found Gdi2 deficiency enhanced cold tolerance and protected against high-fat diet-induced obesity. Mechanistically, *Gdi2*-deficient adipocytes showed increased autophagic flux by promoting the late stage of lipophagy upon β3-AR stimulation. Enhanced lipophagy

led to increased FFA release, which acted as signaling molecules to upregulate thermogenic gene expression, thereby promoting mitochondrial biogenesis and energy expenditure. Notably, RNA-seq confirmed thermogenesis, oxidative phosphorylation, and PPAR signaling as the most significantly enriched pathways. Together, our study identifies GDI2 as a key inhibitor of lipophagy, thereby suppressing WAT browning and adaptive thermogenesis, and suggests GDI2 as a potential therapeutic target for obesity and its associated metabolic diseases.

Materials and methods

Animals

All animal procedures were approved by the Ethics Committee of The First Affiliated Hospital of Shandong First Medical University and performed in accordance with relevant institutional and national guidelines. *Gdi2*$^{flox/+}$ mice were generated using CRISPR/Cas9, with loxP sites inserted into intronic regions flanking exon 2 and exon 3 of the mouse *Gdi2* gene. F1 heterozygous *Gdi2*$^{flox/+}$ mice on a C57BL/6J background were intercrossed to obtain homozygous *Gdi2*$^{flox/flox}$ (hereafter *Gdi2*$^{f/f}$) mice. To achieve adipocyte-specific deletion, *Gdi2*$^{f/f}$ mice were crossed with *Adipoq*-Cre transgenic mice (C001186, The Jackson Laboratory), yielding *Gdi2*$^{flox/flox}$*Adipoq*^{Cre} offspring (hereafter *Gdi2*^{AKO}). Colony maintenance was performed by backcrossing *Gdi2*^{AKO} males with *Gdi2*$^{f/f}$ females. Littermate *Gdi2*$^{f/f}$ mice served as controls. Wild-type C57BL/6J, ob/ob and db/db mice were purchased from Beijing Vital River Laboratory Animal Technology Co., Ltd.

Only male mice were used. For diet-induced obesity (DIO), 8-week-old mice were fed a high-fat diet (HFD; 60% kcal from fat, TP23300, Trophic Animal Feed High-Tech Co., Ltd.)

or normal chow for 12-16 weeks. Body weight, food intake and blood glucose were monitored weekly.

Adaptive thermogenesis was induced by two strategies. In the first, mice were housed under thermoneutral conditions (30 °C) or cold challenge (4 °C) for 14 days, allowed to recover at room temperature for 24 h and then subjected to a cold tolerance test (4°C for 5 h). Rectal temperature was measured hourly using a dual-channel traceable rectal probe (Fisher Scientific). Infrared thermal images were captured at the end of the test. In the second approach, mice received daily intraperitoneal injection of CL316243 (1mg/kg; ab144605, Abcam) or PBS for 7 consecutive days. Unless otherwise noted, mice were group-housed under specific-pathogen-free conditions at 22 °C with a 12 h light/dark cycle and had ad libitum access to food and water.

Human subcutaneous adipose tissue

Subcutaneous adipose tissue biopsies were collected from 21 Chinese subjects (aged 21-38 years) undergoing elective surgery at the Department of Bariatric Surgery, the First Affiliated Hospital of Shandong First Medical University. Body weight and height were recorded, and BMI was calculated accordingly. Total RNA was extracted and quantitative real-time PCR was performed to examine the correlation between *GDI2* mRNA levels and BMI. This study was approved by the Ethics Committee of the First Affiliated Hospital of Shandong First Medical University, and written informed consent was obtained from all participants.

Metabolic phenotyping

Energy expenditure was assessed using a Comprehensive Laboratory Animal Monitoring

System (CLAMS-16, Columbus Instruments). Mice were individually housed in metabolic chambers and monitored continuously for 72 h with free access to food and water. The airflow rate was set at 380 mL/min. Metabolic parameters including oxygen consumption (VO_2), carbon dioxide production (VCO_2), heat production, respiratory exchange ratio (RER), ambulatory activity, and food intake were recorded at 5-min intervals.

For serum analyses, mice were fasted overnight (12 h), and blood was collected from the retro-orbital sinus. Serum was isolated by centrifugation (3000 rpm, 3 min) and stored at -80 °C. FFA (A042-2-1), glycerol (F005-1-1), triglycerides (TG, A110-1-1), glucose (A154-1-1), cholesterol (CHO, A111-1-1), and alanine aminotransferase (ALT, C009-2-1) were measured using commercial kits (Nanjing Jiancheng Bioengineering Institute, China) according to the manufacturer's instructions.

For GTT, mice were fasted for 6 h and injected intraperitoneally with D-glucose (1.5 g/kg; Sigma-Aldrich, D9434). Blood glucose was measured from the tail vein using a glucometer (ACCU-CHEK Active, Roche) at 0, 15, 30, 60, 90, and 120 min. For ITT, mice were fasted for 6 h and injected intraperitoneally with human insulin (0.75 mU/g; Beyotime Biotechnology). Blood glucose was monitored at the same time points.

Ex vivo lipolysis assay

iWAT was freshly dissected from 8-week-old male *Gdi2*^{AKO} and *Gdi2*$^{f/f}$ mice, minced into 3-4 mg fragments, and incubated in high-glucose DMEM containing 10% FBS for 1 h at 37 °C. Medium was then replaced with high-glucose DMEM containing 1% BSA, and fragments were equilibrated for 30 min. Four tissue pieces per well were transferred into a 24-well plate in 1 mL of 1% BSA medium and treated with PBS or CL316243 (1 μM).

Supernatant was collected hourly for up to 6 h, and glycerol and FFA concentrations were determined using commercial colorimetric assay kits. Lipolytic release was normalized to explant dry weight.

Cell culture and induction of differentiation

C3H10T1/2 mesenchymal stem cells (SCSP-506) and 3T3-L1 preadipocytes (GNM-58) were purchased from the Cell Resource Center, Chinese Academy of Sciences. Both cell lines were cultured in DMEM (Gibco, 11966025) supplemented with 10 % fetal bovine serum (FBS; Gibco, A3161001C) and 1 % penicillin-streptomycin (Beyotime, C0222) at 37 °C in a humidified 5 % CO_2 incubator. For adipogenic differentiation, cells were induced for 6-7 days in DMEM containing 10% FBS, dexamethasone (2 μg/mL), insulin (5 μg/mL), rosiglitazone (0.5 μM), IBMX (0.5 mM), T3 (1 nM) and indomethacin (125 μM) for the initial 48 h, followed by medium containing dexamethasone, insulin, rosiglitazone and T3, renewed every other day.

To generate *Gdi2*-knockout (KO) C3H10T1/2 cells, three independent sgRNAs targeting *Gdi2* were cloned into lentiCRISPR v2 (sgRNA sequences in Supplementary data). Lentiviral particles were produced in 293T cells using psPAX2 and pMD2.G. The virus-containing supernatant was collected 48-72 h post-transfection, clarified (3000 rpm, 20 min), and used to infect C3H10T1/2 cells. Transduced cells were selected with puromycin (2 μg/mL; Sangon Biotech, A610593).

SVF cells were isolated from iWAT or BAT of 8-week-old male C57BL/6J mice. Adipose tissues were minced and digested in Hanks' balanced salt solution containing collagenase D (2.5 mg/mL; Sigma, 11088858001) at 37 °C with shaking (220 rpm, 30 min).

The digested mixture was centrifuged, and the pelleted SVF cells were resuspended in culture medium, passed through a 70-μm cell strainer, and plated onto poly-L-lysine-coated (0.1 mg/mL, Sigma, P6282) 6-well plates. The following day, cells were washed with PBS to remove non-adherent cells (designated day -2). Adipogenic differentiation was performed in DMEM/F12 containing 10% FBS, dexamethasone, insulin, rosiglitazone, IBMX, T3, and indomethacin for 3 days, followed by medium without IBMX and indomethacin for 3 days, and then maintained in medium containing dexamethasone, T3, and insulin until day 9. After differentiation, mature adipocytes were treated with CL316243 (1 μM, 6 h) to evaluate the effects of *Gdi2* knockout on LD degradation and thermogenic gene expression.

Autophagy inhibitor treatment

To dissect the autophagy stage affected by *Gdi2* deletion, differentiated sg-NC and *Gdi2*-KO C3H10T1/2 adipocytes were pre-treated for 1 h with the following inhibitors prior to CL316243 stimulation: 3-methyladenine (3-MA, 5 mM; MedChemExpress, HY-19312), an inhibitor of class III PI3K that blocks autophagosome formation; chloroquine (CQ, 10 μM; MedChemExpress, HY-17589A), which neutralizes lysosomal pH; or bafilomycin A1 (Baf A1, 100 nM; MedChemExpress, HY-100558), a vacuolar H^+-ATPase inhibitor preventing autophagosome-lysosome fusion. Inhibitors were maintained throughout the CL316243 stimulation period.

Autophagic flux analysis

Differentiated C3H10T1/2 adipocytes (sg-NC and *Gdi2*-KO) on glass coverslips were infected with an adenovirus expressing tandem mCherry-EGFP-LC3B (ADM-CMV-mCherry-EGFP-LC3B, Vigene Biosciences) at the optimal multiplicity of

infection (MOI). Virus and infection enhancer ADV-HR (Vigene Biosciences) were each added at 5 μL/well. After 12 h, the virus-containing medium was replaced with complete medium, and cells were cultured for an additional 12-36 h. In this reporter, EGFP fluorescence is quenched in acidic lysosomal lumen while mCherry remains stable; therefore, yellow puncta ($GFP^+/mCherry^+$) represent autophagosomes, and red-only puncta ($GFP^-/mCherry^+$) represent autolysosomes. Cells were treated with CL316243, fixed with 4% paraformaldehyde, and imaged with a laser scanning confocal microscope (LSM780, Zeiss). Yellow and red LC3 puncta per cell were quantified manually, and the yellow-to-red puncta ratio was calculated.

Electron microscopy

For TEM, differentiated C3H10T1/2 adipocytes treated with CL316243 (1 μM, 6 h) were harvested by scraping, pelleted, and fixed with 2% paraformaldehyde and 2.5% glutaraldehyde in 0.1 M cacodylate buffer for at least 2 h. Freshly dissected iWAT was cut into 1 mm^3 blocks and fixed in the same solution. Samples were post-fixed with 1% osmium tetroxide (1 h, 25 °C), dehydrated through a graded ethanol series, and embedded in EPON812 resin (Sigma-Aldrich, 45345). Ultrathin sections (60 nm) were stained with uranyl acetate and lead citrate and examined using a JEOL-1200EX TEM operating at 80 kV. Mitochondrial abundance, autophagic vacuoles, and LD morphology were evaluated.

For immunogold labeling, differentiated primary mouse adipocytes were fixed with 4% paraformaldehyde and 0.5% glutaraldehyde to preserve ultrastructure and antigenicity. Cells were permeabilized with 0.1% Triton X-100, blocked with 10% goat serum containing 1% BSA, and incubated with rabbit anti-GDI2 antibody (ABclonal, A8615) overnight at 4 °C,

followed by incubation with 10 nm gold-conjugated goat anti-rabbit IgG for 1 h at room temperature. After washing, the immunogold signal was stabilized by post-fixation with 1% glutaraldehyde, and gold particles were enhanced using Goldenhance EM Plus (2114-8 mL). Samples were post-fixed with 1% osmium tetroxide, dehydrated, infiltrated, and embedded in SPI-Epon812 resin. Ultrathin sections were examined with a JEM-1200EX TEM (JEOL) at 80 kV. Images were recorded with a MORADA-G2 CCD camera.

Histology, immunohistochemistry, and immunofluorescence staining

Adipose tissues were fixed in adipose tissue fixative (Servicebio, G1119), embedded in paraffin, and sectioned at 5 μm. For H&E staining, sections were deparaffinized in xylene, rehydrated through a graded ethanol series, and stained with hematoxylin ((Servicebio, Wuhan, China, G1004)) and eosin (Servicebio, G1002).

For immunostaining, paraffin sections were deparaffinized, rehydrated, and subjected to antigen retrieval in Tris-EDTA buffer (pH 9.0, Beyotime, P0084) by microwave heating. For UCP1 immunohistochemistry, endogenous peroxidase was blocked with 3% H_2O_2 for 10 min and then with normal goat serum for 15 min. Sections were incubated with rabbit anti-UCP1 (Proteintech, 23673-1-AP) overnight at 4 °C, followed by biotinylated goat anti-rabbit IgG and streptavidin-HRP (ZSGB-BIO, SP-9002). Signals were developed with DAB and counterstained with hematoxylin. For F4/80 immunofluorescence, antigen-retrieved eWAT sections were blocked with 10% goat serum for 1 h, incubated with rabbit anti-F4/80 antibody (Proteintech, 28463-1-AP) overnight at 4 °C, and detected with Alexa Fluor-conjugated secondary antibody (1:500, Life Technologies, 1 h, 37 °C, dark). Sections were mounted with DAPI-containing medium and imaged with a confocal microscope (LSM780, Zeiss).

For immunofluorescence staining of cultured adipocytes, differentiated primary adipocytes or C3H10T1/2 cells on coverslips were fixed with 4% paraformaldehyde for 30 min, permeabilized with 0.2% Triton X-100 for 30 min, and blocked with 10% goat serum for 1 h. Cells were incubated overnight at 4 °C with primary antibodies against LC3B (Proteintech, 14600-1-AP), PLIN1 (Proteintech, 27716-1-AP) or GDI2 (ABclonal, A8615), followed by Alexa Fluor® 488- or 594-conjugated secondary antibodies (1 h, 37 °C; Life Technologies). LDs were visualized with BODIPY 493/503 (ThermoFisher Scientific, D3922). Coverslips were mounted with DAPI-containing medium and imaged with a confocal microscope (LSM780, Zeiss). Images were analyzed with ImageJ.

RNA-seq analysis

Total RNA was extracted from the iWAT of cold-exposed *Gdi2*^{AKO} and *Gdi2*$^{f/f}$ mice. Polyadenylated mRNA was enriched with oligo(dT) magnetic beads and fragmented. Double-stranded cDNA was synthesized using random hexamer primers and M-MuLV reverse transcriptase, followed by end repair, A-tailing, and Illumina adapter ligation. Libraries were size-selected (370-420 bp) with AMPure XP beads, amplified by PCR, purified, and quantified with a Qubit 2.0 Fluorometer and Agilent 2100 Bioanalyzer. Qualified libraries were pooled and sequenced on an Illumina platform to generate 150 bp paired-end reads.

Raw reads were filtered to remove adapter-containing reads, reads with uncalled bases, and low-quality reads (those with > 50 % of bases having Qphred ≤ 5). Clean reads were aligned to the mouse reference genome (GRCm38) using HISAT2 (v2.0.5). Read counts were obtained with featureCounts (v1.5.0-p3), and gene expression was expressed as fragments per kilobase of transcript per million mapped reads (FPKM). Genes with *p value* < 0.05 and

287 $|log_2FC| > 1$ were identified with DESeq2 (v1.20.0). Gene Ontology (GO) and KEGG
288 pathway enrichment were conducted with clusterProfiler (v3.8.1). RNA-seq data have been
289 deposited in the Gene Expression Omnibus (GEO) under accession number GSE336061.

290 **Statistical analysis**

291 All experiments were independently repeated at least three times. Data are expressed as
292 mean ± SEM. Two-group comparisons were performed using an unpaired two-tailed Student's
293 *t*-test. For multiple groups, a one-way analysis of variance (ANOVA) was used, followed by
294 Bonferroni's post hoc test. For two independent variables, a two-way ANOVA was applied,
295 followed by Bonferroni's multiple comparison test. All analyses were conducted using
296 GraphPad Prism 8.0 (GraphPad Software, San Diego, CA, USA). A P values < 0.05 were
297 considered statistically significant, with significance levels denoted as $*P < 0.05$, $**P < 0.01$,
298 $***P < 0.001$, and $****P < 0.0001$.

299 **Results**

300 **Identification of adipose GDI2 as a metabolic signature.**

301 To explore the role of GDI2 in adipocytes, we examined its expression during adipogenic
302 differentiation. Immunoblot analysis revealed that GDI2 protein levels progressively
303 increased throughout the differentiation of 3T3-L1 preadipocytes, C3H10T1/2 mesenchymal
304 stem cells, and primary mouse adipocytes (Fig. 1A-C). Confocal immunofluorescence
305 imaging of differentiated primary adipocytes showed that GDI2 was enriched at the periphery
306 of BODIPY-positive LDs and partially colocalized with the LD-coating protein PLIN1 (Fig.
307 1D). To further resolve its subcellular distribution, we performed immunogold electron
308 microscopy. GDI2 was predominantly detected in the cytoplasm, with additional labeling

observed on LDs, at endoplasmic reticulum (ER)-LD contact sites, within ER vacuoles, and on autolysosome-like structures, suggesting its possible involvement in LD dynamics and autophagic degradation (Fig. 1E).

We next examined the association between GDI2 and obesity using leptin-deficient (*ob/ob*), leptin receptor-deficient (*db/db*), and diet-induced obesity (DIO) mouse models. GDI2 expression was significantly upregulated in both inguinal white adipose tissue (iWAT) and brown adipose tissue (BAT) of obese mice, and its levels were inversely correlated with UCP1 expression (Fig. 1F-H and Supplementary Fig.1A-C). Given that cold exposure or β3-AR activation promote WAT browning and adaptive thermogenesis, we subjected mice to cold exposure (4°C for 7 days) or intraperitoneal injection of the β3-AR agonist (CL316243 for 7 days). Under both thermogenic stimuli, GDI2 expression was markedly reduced in iWAT and BAT, again showing a negative correlation with UCP1 levels (Fig. 1I-J and Supplementary Fig.1D-E). We further analyzed human subcutaneous adipose tissue and found GDI2 mRNA levels were elevated in obese subjects and positively correlated with BMI (Fig. 1K). Consistently, analysis of the publicly available GSE162653 dataset confirmed higher GDI2 expression in WAT of obese individuals (Fig. 1L). In contrast, the expression of *GDI1*, a closely related member of the GDI family, was not significantly different between lean and obese individuals in the same dataset (Supplementary Fig. 1F). Furthermore, immunoblot analysis of iWAT and BAT from HFD-fed mice showed that GDI1 protein levels were comparable to those in chow-diet controls (Supplementary Fig. 1G-H), indicating that the obesity-associated upregulation is specific to GDI2. Collectively, GDI2 emerges as a potential key regulator in adipose tissue metabolism.

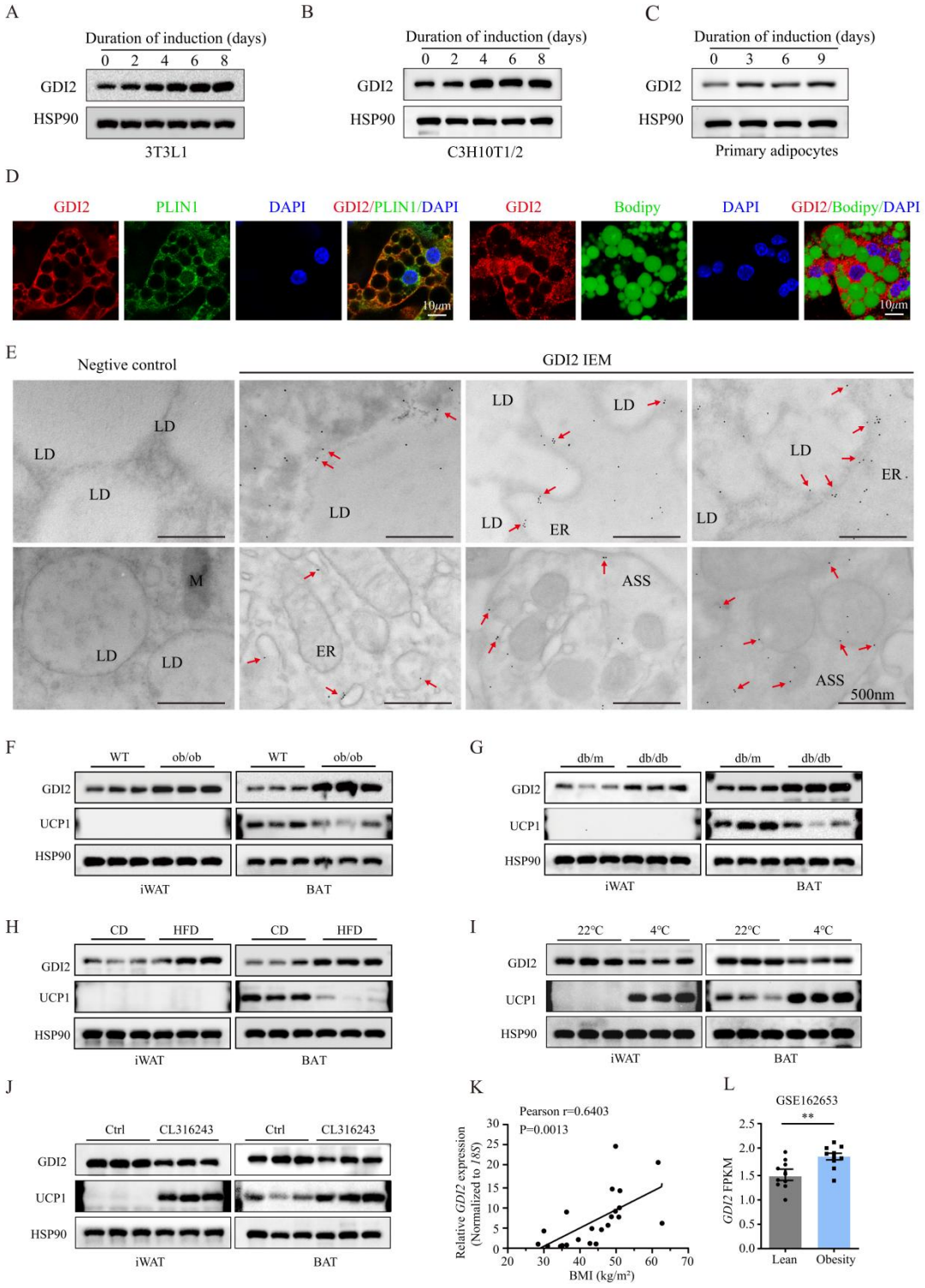


Fig. 1 Adipose GDI2 is upregulated in obesity and suppressed by thermogenic stimuli.

(A-C) Representative immunoblots of GDI2 and HSP90 (loading control) during adipogenic

differentiation of 3T3-L1 preadipocytes (A), C3H10T1/2 mesenchymal stem cells (B), and primary mouse adipocytes (C). Days post-induction are indicated. (D) Confocal immunofluorescence images of differentiated primary adipocytes stained for GDI2 (red) and PLIN1 (green), or GDI2 (red) and BODIPY (green). Scale bar, 10 μm. (E) Immunogold electron microscopy of GDI2 in differentiated primary adipocytes. Gold particles (arrowheads) localize to LD, endoplasmic reticulum-LD contact sites, ER vacuoles, and autolysosomes (ASS). Negative control was processed identically except that the primary antibody was replaced with PBS. Scale bar, 500 nm. (F-H) Representative immunoblots of GDI2, UCP1, and HSP90 in iWAT and BAT from ob/ob mice (F), db/db mice (G), and mice fed a high-fat diet (HFD) or normal chow diet (CD) (H), n = 6 independent experiments, each lane represents an individual mouse. (I-J) Representative immunoblots of GDI2 and UCP1 in iWAT and BAT of wild-type mice housed at room temperature (RT, 22 °C) or exposed to cold (4 °C) for 14 days (I), and of mice injected intraperitoneally with PBS (vehicle) or CL316243 for 7 days (J), n = 6 per group. (K) Spearman correlation between *GDI2* mRNA levels in human subcutaneous adipose tissue and BMI (n = 21 individuals). The Spearman correlation coefficient r and P value are indicated. (L) *GDI2* expression in subcutaneous adipose tissue of lean (n = 10) and obese (n = 10) individuals from the GSE162653 dataset. $^{**}P < 0.001$ by two-tailed unpaired Student's *t*-test.

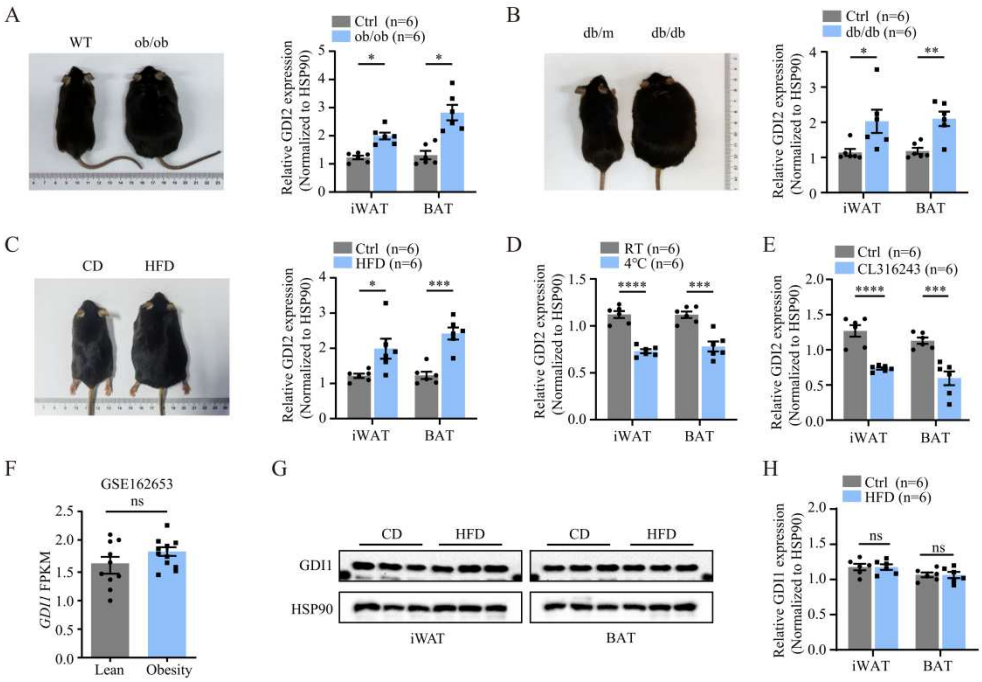


Fig. S1 GDI2 is upregulated in obese adipose tissue and downregulated by thermogenic activation, while GDI1 remains unchanged.

(A-C) Representative gross morphology (left) and quantification of GDI2 protein levels normalized to HSP90 (right) in iWAT and BAT from ob/ob and WT controls (A), db/db and db/m mice (B), and mice fed a HFD or CD for 16 weeks (C). n = 6 per group. Corresponding immunoblot images are shown in Fig. 1F-H. (D-E) Quantification of GDI2 protein levels in iWAT and BAT from wild-type mice housed at room temperature (RT, 22 °C) or exposed to cold (4 °C) for 14 days (D), and from mice injected intraperitoneally with PBS (vehicle) or CL316243 for 7 days (E). n = 6 per group. Corresponding immunoblot images are presented in Fig. 1I-J. (F) *GDI1* mRNA expression in subcutaneous adipose tissue of lean (n = 10) and obese (n = 10) individuals from the GSE162653 dataset. (G) Representative immunoblots of GDI1 and HSP90 in iWAT and BAT from mice fed a HFD or CD for 16 weeks. (H) Quantification of GDI1 protein levels from G (n = 6 per group). All bar graphs are

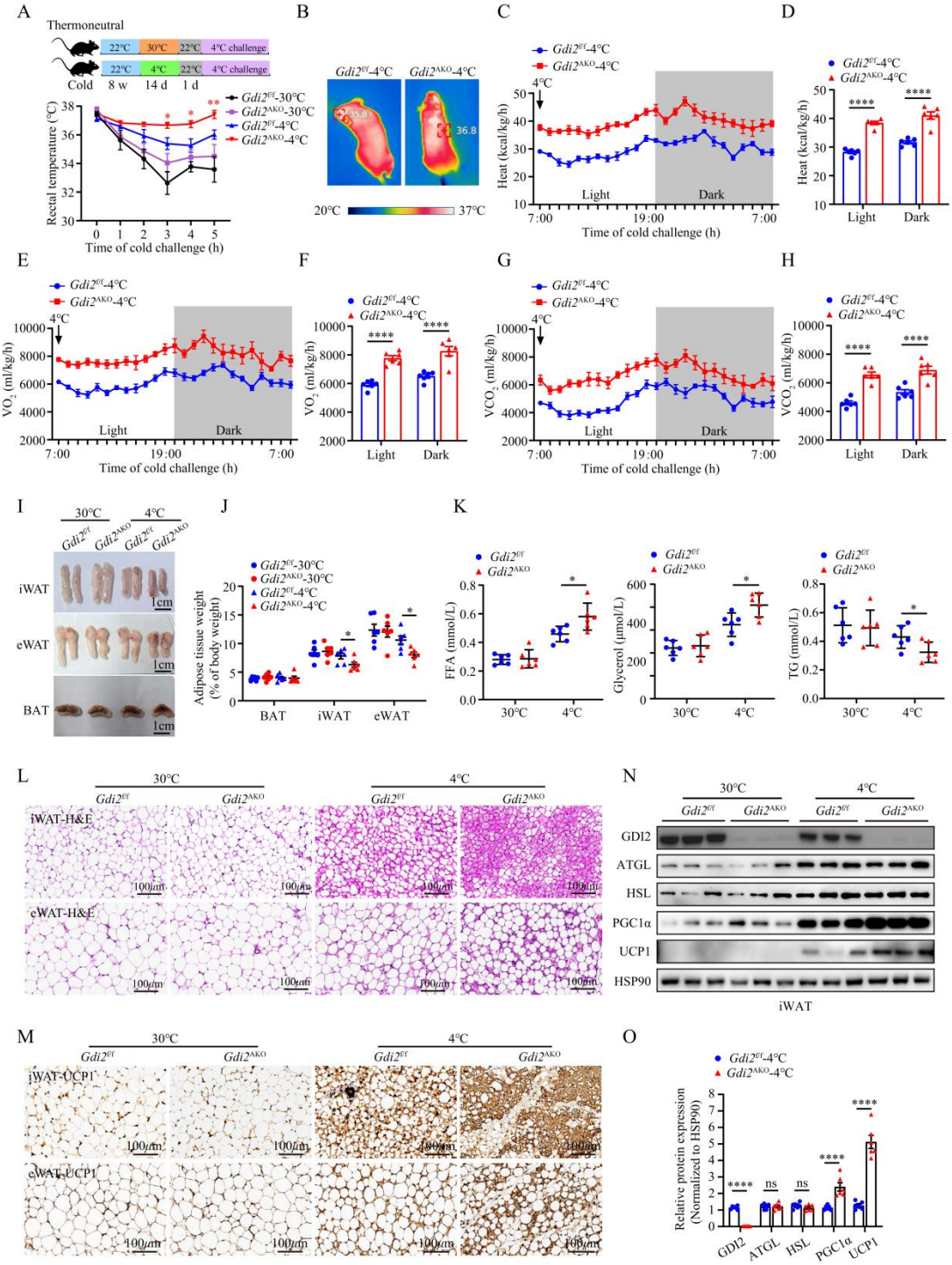
presented as mean ± s.e.m. Statistical comparisons were performed using unpaired two-tailed Student's *t*-test. *$P < 0.05$, **$P < 0.01$, ***$P < 0.001$, ****$P < 0.0001$, n.s., not significant.

Adipocyte *Gdi2* deficiency promotes cold-induced WAT browning and adaptive thermogenesis.

To define the physiological role of *Gdi2* in adipose tissue *in vivo*, we generated adipocyte-specific *Gdi2* knockout ($Gdi2^{AKO}$) mice by crossing $Gdi2^{flox/+}$ mice with *Adipoq*-Cre transgenic mice (Supplementary Fig. 2A-C). Immunoblot analysis confirmed robust and selective depletion of GDI2 in iWAT, eWAT, and BAT of $Gdi2^{AKO}$ mice, with hepatic GDI2 expression unaffected (Supplementary Fig. 2D). The completeness of adipocyte-specific deletion was further verified in mature adipocytes differentiated *in vitro* from the SVF of iWAT and BAT, in which GDI2 protein was undetectable (Supplementary Fig. 2E). Under standard chow diet, 8-week-old $Gdi2^{AKO}$ mice and littermate controls ($Gdi2^{f/f}$) showed no significant differences in body weight, adipose tissue weights, or serum triglyceride (TG), FFA, and glycerol (Supplementary Fig. 2F-I).

We next examined whether *Gdi2* participates in cold-induced adaptive thermogenesis. $Gdi2^{AKO}$ and $Gdi2^{f/f}$ mice were housed at thermoneutral (30°C) or cold (4°C) for 14 days, with 30°C serving as a baseline to minimize effects of shivering thermogenesis. Under thermoneutral conditions, $Gdi2^{AKO}$ mice showed no differences in body weight, metabolic rates (O_2 consumption, CO_2 production, heat generation), respiratory exchange ratio (RER), or food intake (Supplementary Fig. 3A-J). Following the 14-day acclimation, mice were allowed to recover at room temperature for 24 h and then subjected to an acute cold challenge (4°C) for rectal temperature measurement. As expected, cold-trained mice maintained higher

core temperatures than thermoneutral-housed mice. Notably, cold-trained *Gdi2*^{AKO} mice exhibited significantly higher rectal temperatures, indicating that adipocyte *Gdi2* deficiency augments thermogenic capacity (Fig. 2A-B and Supplementary Fig.3K). Cold-exposed *Gdi2*^{AKO} mice demonstrated significantly elevated O_2 consumption, CO_2 production, and heat generation, despite no differences in body weight, food intake, or RER (Fig. 2C-H and Supplementary Fig.3L-O). The weights of iWAT and eWAT were significantly reduced in *Gdi2*^{AKO} mice, whereas BAT weight remained unchanged (Fig. 2I-J). Serum analysis revealed increased FFAs and glycerol levels with decreased TGs in cold-exposed *Gdi2*^{AKO} mice (Fig. 2K). H&E staining revealed a shift from large unilocular to small multilocular LDs in iWAT and eWAT of *Gdi2*^{AKO} mice, and UCP1 immunostaining confirmed an increased proportion of UCP1-positive beige adipocytes (Fig. 2L-M and Supplementary Fig. 3P). Immunoblot analysis of iWAT revealed upregulation of the thermogenic effectors PGC1α and UCP1, whereas ATGL and HSL levels remained unchanged (Fig. 2N-O). In BAT, no significant differences were observed in LD morphology after thermoneutral or cold exposure by H&E staining (Supplementary Fig. 4A-B). Collectively, our results demonstrate that adipocyte *Gdi2* deficiency promotes cold-induced WAT browning and adaptive thermogenesis.



406

407 **Fig. 2 Adipocyte *Gdi2* deficiency promotes cold-induced WAT browning and**

408 **adaptive thermogenesis.**

409 (A) Rectal temperature measurements during an acute cold challenge (4 °C, 5 h) in *Gdi2*^{AKO}

410 and *Gdi2*$^{f/f}$ mice that had been previously housed at thermoneutrality (30 °C) or cold (4 °C)

411 for 14 days followed by 24 h recovery at room temperature (n = 6 per group). (B)
412 Representative infrared thermal images of cold-trained *Gdi2*^{AKO} and *Gdi2*$^{f/f}$ mice after 5 h of
413 acute cold exposure. (C-H) Hourly profiles of heat production (C-D), oxygen consumption
414 (VO_2) (E-F), and carbon dioxide production (VCO_2) (G-H) in cold-trained mice monitored
415 over 24 h at 4 °C (n = 6 per genotype). White and gray areas in the graphs indicate day and
416 night, respectively. (I) Gross appearance of iWAT, eWAT, and BAT depots from
417 cold-exposed *Gdi2*^{AKO} and *Gdi2*$^{f/f}$ mice. Scale bar, 1 cm. (J) Quantification of adipose tissue
418 weights normalized to body weight (n = 6 per genotype). (K) Serum levels of FFA, glycerol,
419 and TG in mice housed at thermoneutrality or after cold exposure (n = 6 per group). (L)
420 Representative H&E staining of iWAT and eWAT sections. Scale bar, 100 μm. (M)
421 Representative UCP1 immunohistochemistry of iWAT and eWAT sections. Scale bar, 100 μm.
422 (N) Immunoblot analysis of GDI2, ATGL, HSL, PGC1α, and UCP1 in iWAT from
423 cold-exposed *Gdi2*^{AKO} and *Gdi2*$^{f/f}$ mice. Each lane represents an individual mouse (n = 6 per
424 genotype). (O) Quantification of GDI2, ATGL, HSL, PGC1α and UCP1 protein levels from
425 (N) normalized to HSP90 (n = 6 per genotype). Statistical comparisons were performed
426 between *Gdi2*^{AKO} and *Gdi2*$^{f/f}$ mice: A, C-H, K, two-way ANOVA with Bonferroni's post hoc
427 test; J, O, unpaired two-tailed Student's *t*-test. **P* < 0.05, ***P* < 0.01, ****P* < 0.001, *****P* <
428 0.0001. All data are presented as mean ± s.e.m.

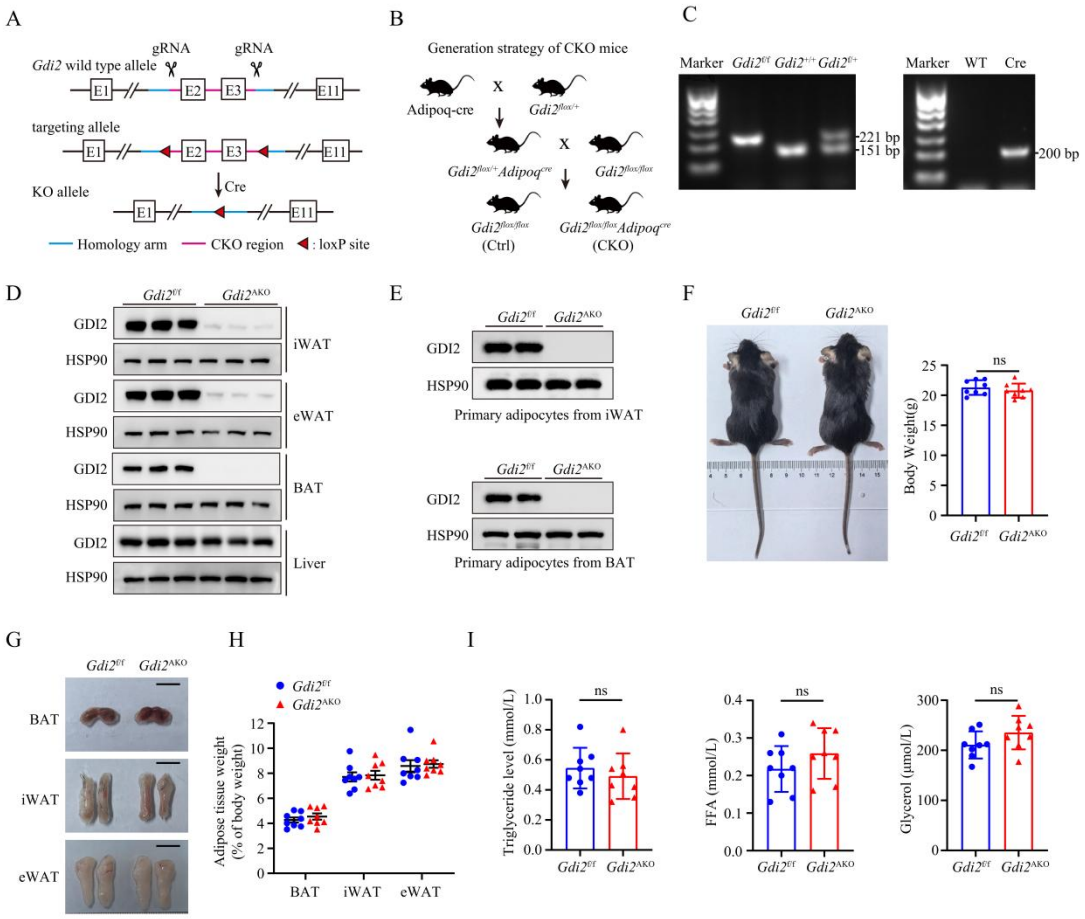


Fig. S2 Generation and basal metabolic characterization of adipocyte-specific *Gdi2* knockout mice.

(A) Schematic illustration of the strategy used to generate the *Gdi2* conditional knockout allele. (B) Breeding scheme for producing adipocyte-specific *Gdi2* knockout ($Gdi2^{AKO}$) mice and littermate control ($Gdi2^{f/f}$) mice. (C) Representative agarose gel electrophoresis images for genotyping, showing amplification products of the floxed *Gdi2* allele and the *Cre* transgene. (D) Western blot analysis of GDI2 and HSP90 (loading control) in iWAT, eWAT, BAT, and liver from $Gdi2^{AKO}$ and control mice, demonstrating efficient and adipose-selective depletion of GDI2. (E) SVF cells isolated from iWAT and BAT of $Gdi2^{AKO}$ mice were differentiated into mature adipocytes *in vitro*, and GDI2 depletion efficiency was

assessed by western blot. GDI2 protein was undetectable in the resulting adipocytes. (F) Representative gross appearance and body weight quantification of 8-week-old mice (n = 6 per genotype). (G-H) Representative images of adipose tissue depots and quantification of adipose tissue weights normalized to body weight. (I) Serum levels of TG, FFA, and glycerol in 8-week-old *Gdi2*^{AKO} and *Gdi2*$^{f/f}$ mice. For panels F-I, statistical significance was determined by unpaired two-tailed Student's *t*-test. All data are shown as mean ± s.e.m. **P* < 0.05, ***P* < 0.01, ****P* < 0.001, *****P* < 0.0001, n.s., not significant.

Adipocyte *Gdi2* deficiency potentiates β3-AR-induced WAT browning and stimulated lipolysis.

Cold-induced catecholamine release from sympathetic nerve terminals engages β3-AR signaling to initiate the thermogenic program in adipocytes [5]. To investigate whether adipocyte *Gdi2* directly modulates β3-AR-driven activation of adaptive thermogenesis, we administered CL316243 or PBS intraperitoneally to *Gdi2*^{AKO} and *Gdi2*$^{f/f}$ mice for 7 consecutive days. Mice were subsequently subjected to an acute cold challenge (4°C), and core body temperature was monitored by rectal probe. Notably, CL316243-treated *Gdi2*^{AKO} mice exhibited significantly higher rectal temperatures, indicating enhanced cold tolerance upon β3-AR stimulation (Fig. 3A). Consistently, *Gdi2*^{AKO} mice showed a pronounced reduction in iWAT and eWAT weights with no change in BAT (Fig. 3B-C). Increased WAT browning in *Gdi2*^{AKO} mice was revealed by H&E staining and UCP1 immunostaining, revealing a higher abundance of multilocular, UCP1-positive beige adipocytes in iWAT and eWAT (Fig. 3D-E). Immunoblot analysis of iWAT from CL316243-treated *Gdi2*^{AKO} mice showed upregulation of PGC1α and UCP1, with no

462 alteration in ATGL and HSL (Fig. 3F). *Gdi2*^{AKO} mice displayed elevated serum FFAs and
463 glycerol, suggesting enhanced substrate delivery to thermogenesis (Fig. 3G-H). To directly
464 assess whether adipocyte *Gdi2* deficiency affects stimulated lipolysis, we performed *ex*
465 *vivo* lipolysis assays using iWAT explants from *Gdi2*^{AKO} and *Gdi2*$^{f/f}$ mice. Explants were
466 stimulated with either CL316243 or Forskolin (a direct activator of adenylyl cyclase), and the
467 rates of glycerol and FFA release were quantified. Consistently, iWAT explants
468 from *Gdi2*^{AKO} mice exhibited elevated glycerol and FFA release upon CL316243 or Forskolin
469 stimulation, while baseline release upon PBS was indistinguishable (Fig. 3I-L). In BAT, no
470 significant differences were observed in LD morphology after CL316243 administration by
471 H&E staining (Supplementary Fig. 4C). Collectively, our results reveal that adipocyte *Gdi2*
472 deficiency potentiates β3-AR-induced WAT browning and stimulated lipolysis, augmenting
473 adaptive thermogenesis.

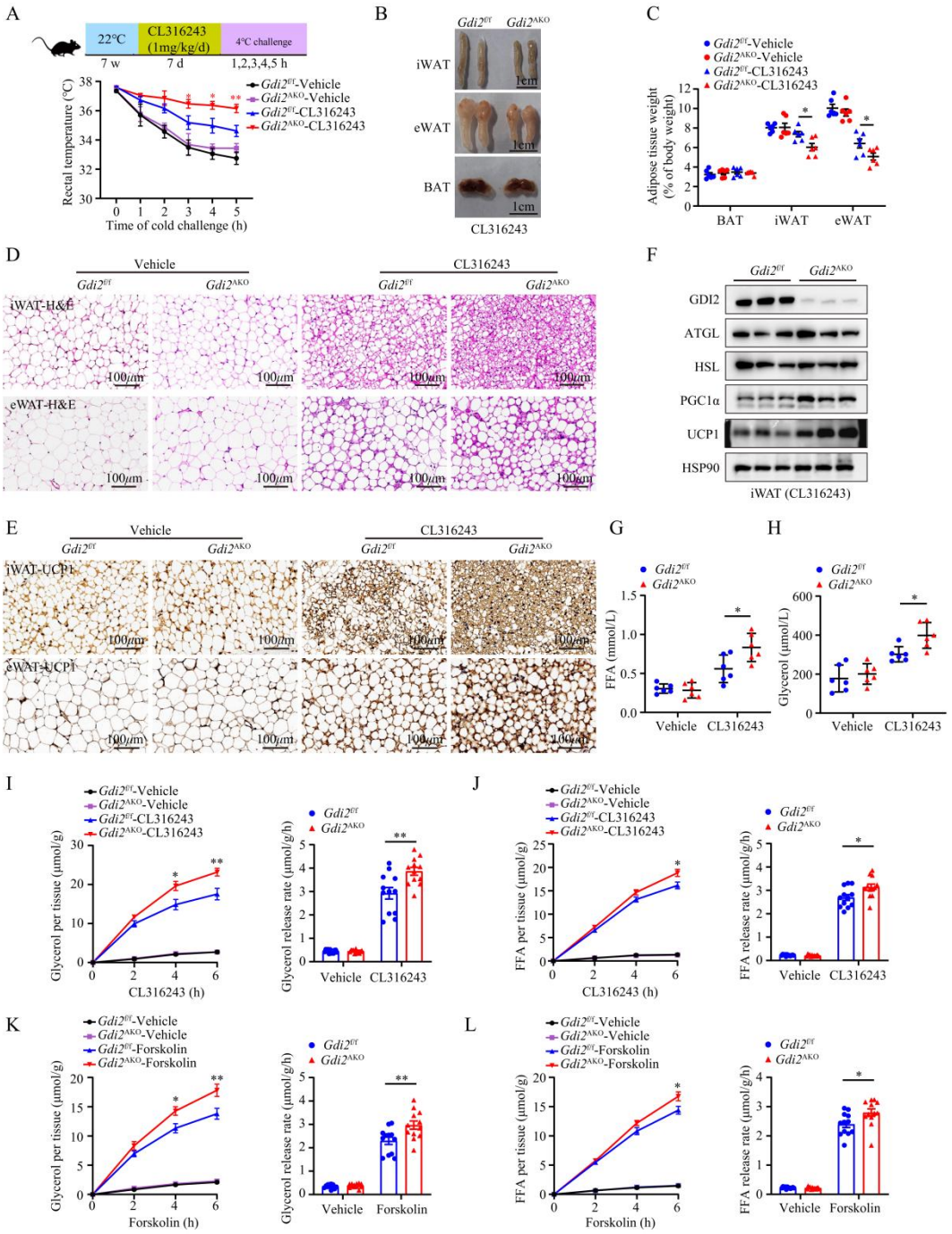


Fig. 3 Adipocyte *Gdi2* deficiency potentiates β3-AR-induced WAT browning and stimulated lipolysis.

(A) Rectal temperature profiles of *Gdi2*^{AKO} and *Gdi2*$^{f/f}$ mice during an acute cold challenge (4 °C, 5 h) following 7-day daily intraperitoneal injection of CL316243 or PBS (n = 6 per group). (B) Gross morphology of iWAT, eWAT and BAT depots after the 7-day treatment.

480 Scale bar, 1 cm. (C) Adipose tissue weights normalized to body weight (n = 6 per genotype).
481 (D) Representative H&E staining of iWAT and eWAT sections. Scale bar, 100 μm. (E)
482 Representative UCP1 immunohistochemistry of iWAT and eWAT sections. Scale bar, 100 μm.
483 (F) Immunoblot analysis of GDI2, ATGL, HSL, PGC1α, and UCP1 in iWAT from
484 CL316243-treated *Gdi2*^{AKO} and *Gdi2*$^{f/f}$ mice. Each lane represents an individual mouse (n = 6
485 per genotype). (G-H) Serum levels of FFA (G), glycerol (H) levels in mice treated with PBS
486 or CL316243 for 7 days (n = 6 per group). (I-L) *Ex vivo* lipolysis assays of iWAT explants.
487 Explants were stimulated with PBS or CL316243 (1 μM) (I-J), as well as PBS or forskolin
488 (10 μM) (K-L). Each panel shows the time-course of glycerol or FFA release per tissue weight
489 (left) and the corresponding calculated release rate (right). n = 12 explants from four mice per
490 genotype. Statistical comparisons: C, unpaired two-tailed Student's *t*-test; A, G-J, two-way
491 ANOVA with Bonferroni's post hoc test. *P < 0.05, **P < 0.01, ***P < 0.001, ****P <
492 0.0001. All data are presented as mean ± s.e.m.

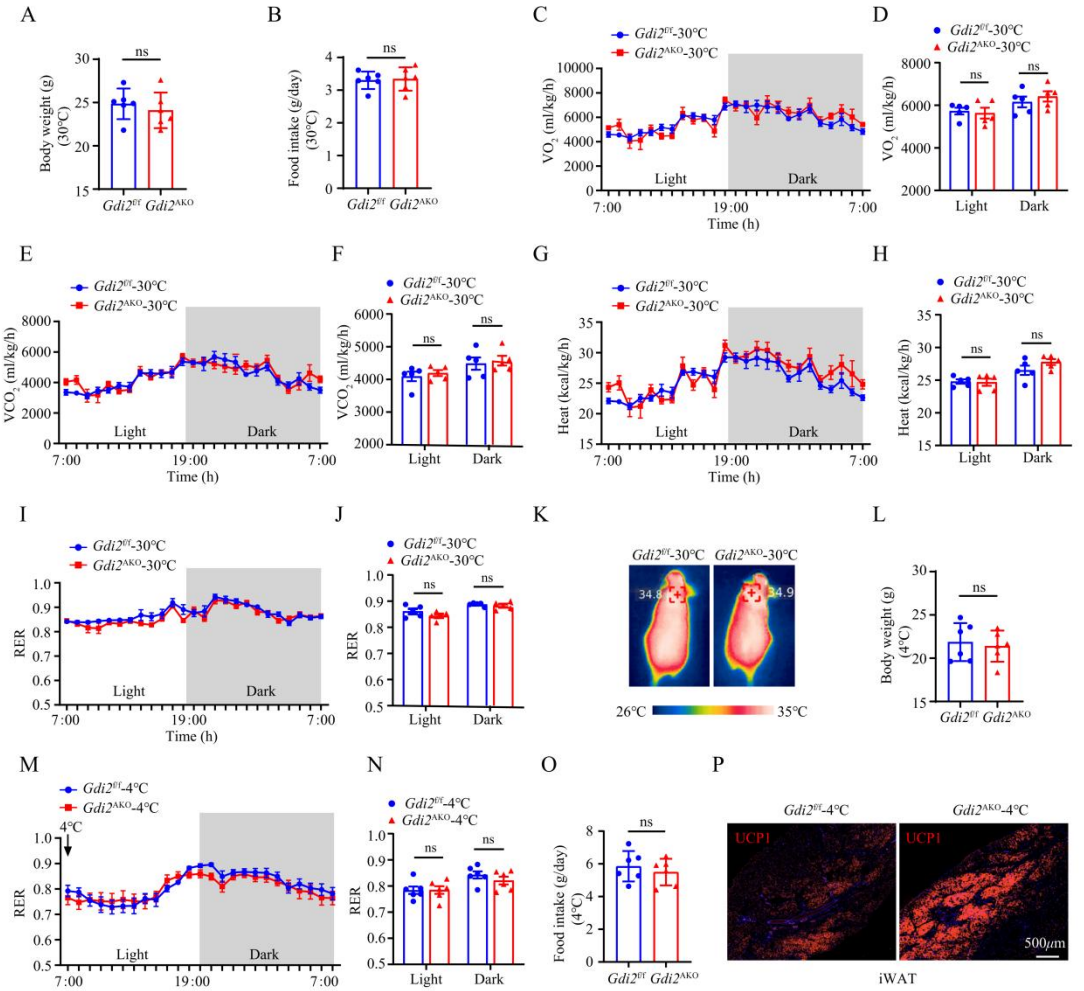


Fig. S3 Metabolic characterization of *Gdi2*^{AKO} and *Gdi2*$^{f/f}$ mice under thermoneutral and cold exposure conditions.

(A) Body weight of *Gdi2*^{AKO} and *Gdi2*$^{f/f}$ mice after 14 days of housing at thermoneutrality (30°C). (B) Food intake under thermoneutral conditions. (C-D) O_2 consumption (VO_2) under thermoneutral conditions, shown as 24-h profiles (C) and average values during light and dark phases (D), n = 5 per genotype. (E-F) CO_2 production (VCO_2) under thermoneutral conditions, presented as 24-h traces (E) and average values during light and dark phases (F). (G-H) Heat production under thermoneutral conditions, displayed as 24-h kinetics (G) and mean light/dark values (H). (I-J) Respiratory exchange ratio (RER) under thermoneutral conditions,

represented by 24-h recordings (I) and light/dark phase averages (J). (K) Representative infrared thermal images of thermoneutrality-trained *Gdi2*^{AKO} and *Gdi2*$^{f/f}$ mice after 5 h of acute cold exposure at 4°C. (L) Body weight of *Gdi2*^{AKO} and *Gdi2*$^{f/f}$ mice after 14 days of cold exposure (4°C). (M-N) RER in cold-trained mice monitored over 24 h at 4 °C (n = 6 per genotype), depicted as 24-h profiles (M) and mean light/dark phase values (N). (O) Food intake under 4 °C conditions. (P) UCP1 immunofluorescence staining of iWAT from cold-exposed mice. Scale bar, 500 μm. Statistical comparisons were performed between *Gdi2*^{AKO} and *Gdi2*$^{f/f}$ mice: A-B, L, O, unpaired two-tailed Student's *t*-test; C-J and M-N were analyzed by two-way ANOVA with Bonferroni's post hoc test. All data are presented as mean ± s.e.m. **P* < 0.05, ***P* < 0.01, ****P* < 0.001, *****P* < 0.0001, n.s., not significant.

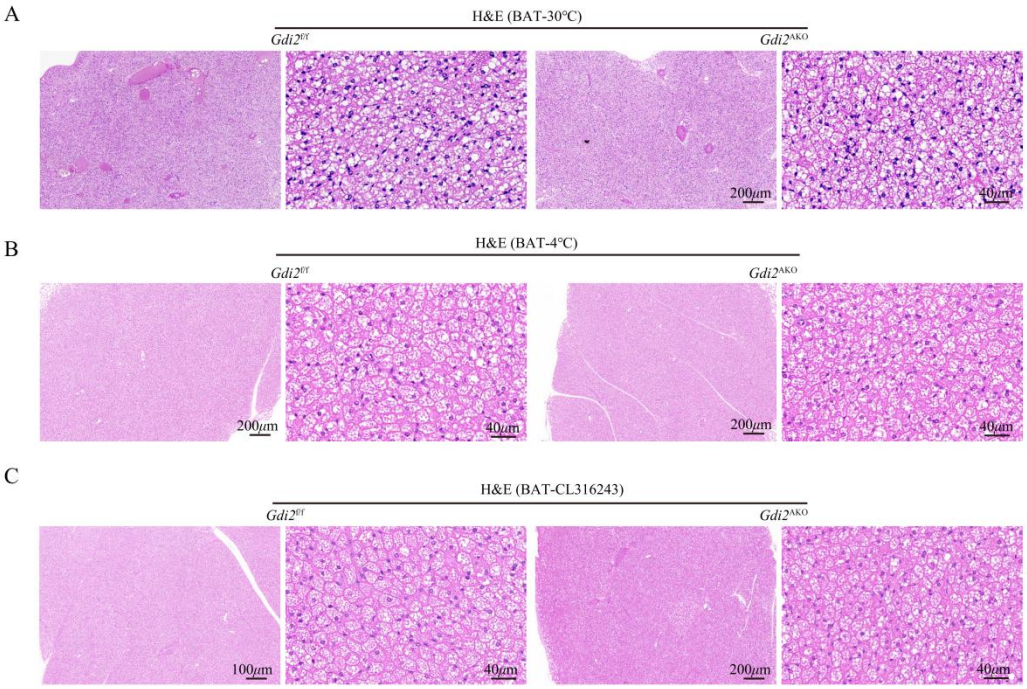


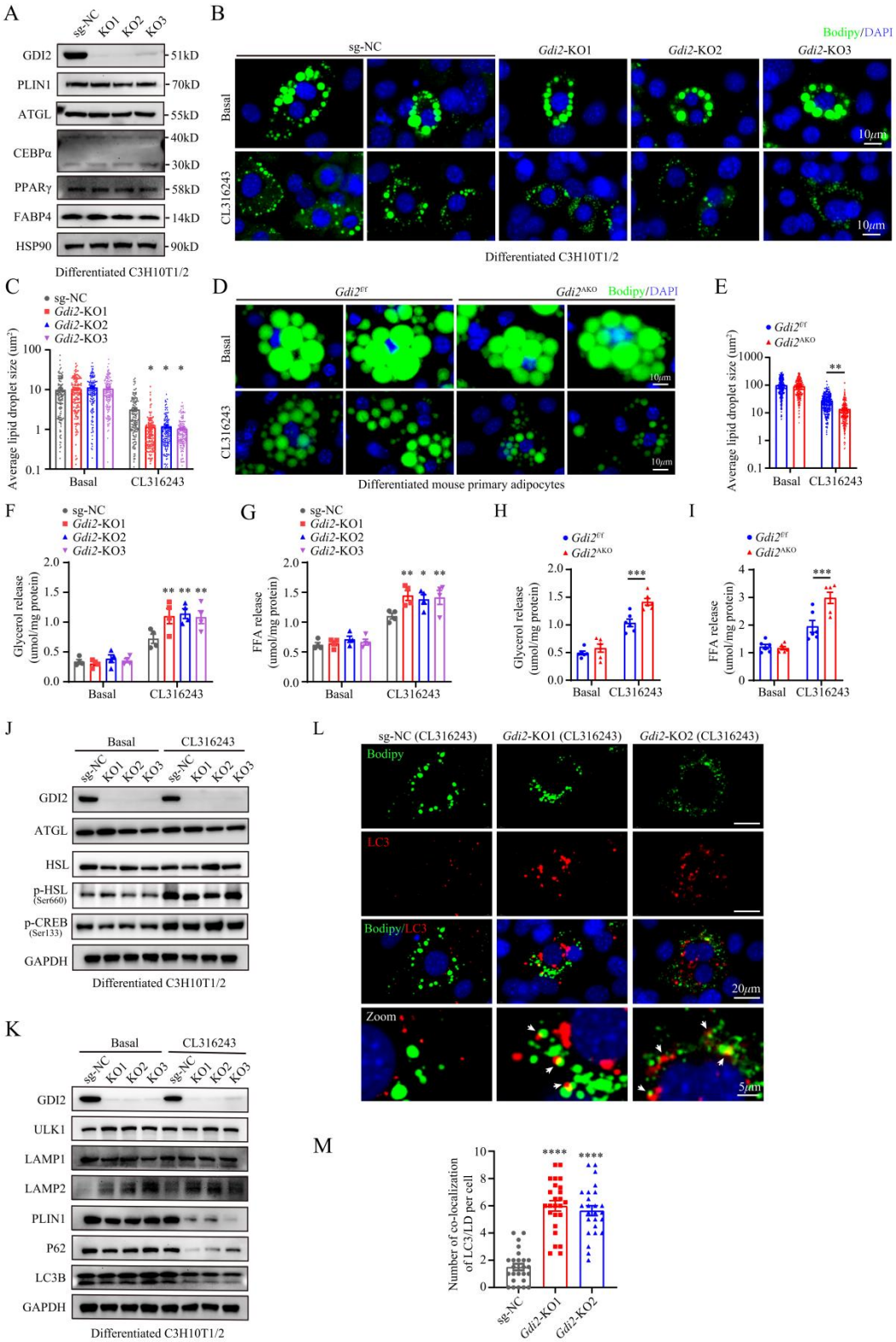
Fig. S4 BAT morphology in *Gdi2*^{AKO} and *Gdi2*$^{f/f}$ mice under thermoneutral, cold exposure, or β3-AR stimulation.

(A) Representative H&E staining of BAT sections from mice housed at thermoneutrality (30°C) for 14 days. (B) Representative H&E staining of BAT after 14 days of cold exposure (4°C). (C) H&E staining of BAT following CL316243 treatment.

Lipophagy is the main driver of enhanced LD degradation in *Gdi2*-deficient adipocytes

We next sought to define the role of *Gdi2* in stimulated lipolysis. We utilized CRISPR-Cas9 to generate three independent *Gdi2* knockout (KO) C3H10T1/2 cell lines. Induction of adipogenic differentiation revealed that *Gdi2* depletion did not perturb the expression of key adipogenic proteins, including PLIN1, ATGL, CEBPα, PPARγ, and FABP4, indicating that *Gdi2* is dispensable for adipocyte maturation (Fig. 4A). Similarly, BrdU incorporation assays confirmed that *Gdi2* loss did not alter the proliferative capacity of the SVF (Supplementary Fig. 5A-B). We then assessed stimulated lipolysis in differentiated C3H10T1/2 cells or primary adipocytes. Upon CL316243 stimulation, *Gdi2*-KO adipocytes exhibited a pronounced reduction in LD size relative to controls, suggesting enhanced lipolysis (Fig. 4B-E). This was corroborated by elevated glycerol and FFA release in the culture medium of both *Gdi2*-KO C3H10T1/2 cells and primary adipocytes derived from $Gdi2^{AKO}$ mice (Fig. 4F-I). To dissect the underlying mechanism, we first examined the canonical cAMP-PKA axis. Immunoblot analysis revealed that CL316243 induced comparable phosphorylation of CREB and HSL in both sg-NC and *Gdi2*-KO cells, with no alterations in total ATGL and HSL (Fig. 4J). Thus, enhanced lipolysis in *Gdi2*-deficient adipocytes is independent of neutral lipolysis. Given the emerging role of lysosome acid lipolysis induced by lipophagy in LD turnover, we next monitored autophagic flux.

539 Notably, *Gdi2*-KO C3H10T1/2 cells displayed a concurrent decrease in the autophagy
540 substrate P62 and the lipidated form of LC3B (LC3B-II), accompanied by reduced levels of
541 the LD coat protein PLIN1, and elevated expression of the lysosomal membrane protein
542 LAMP2 (but not LAMP1) (Fig. 4K). These changes pointed to accelerated autophagic flux
543 with enhanced lysosomal clearance. Core autophagy initiation factor ULK1 remained
544 unchanged. The decrease of PLIN1 in *Gdi2*-deficient adipocytes was also corroborated by
545 immunofluorescence imaging (Supplementary Fig. 5C). To directly visualize whether the
546 autophagic machinery was targeting LDs, we performed confocal imaging of LC3B and
547 BODIPY. Under CL316243 stimulation, *Gdi2*-KO cells exhibited an increase in LC3B
548 colocalization with BODIPY-labeled LDs compared to sg-NC controls (Fig. 4L-M).
549 Notably, LC3B-positive structures in *Gdi2*-KO cells frequently appeared as enlarged clustered
550 formations enveloping LDs, a morphological hallmark of active lipophagy. Collectively, our
551 results establish that lipophagy is the principal driver of enhanced LD hydrolysis in
552 *Gdi2*-deficient adipocytes.



553

554 **Fig. 4 Lipophagy is the main driver of enhanced LD degradation in**

555 ***Gdi2*-deficient adipocytes.**

556 (A) Immunoblot analysis of the indicated adipogenic markers in differentiated sg-NC

and *Gdi2*-KO C3H10T1/2 cells. (B) BODIPY staining of LDs in sg-NC and *Gdi2*-KO adipocytes treated with PBS or CL316243. Scale bar, 10 μm. (C) Quantification of LD diameter from (B), n = 150 LDs pooled from three independent experiments. (D) BODIPY staining of primary adipocytes treated with PBS or CL316243 from $Gdi2^{AKO}$ and $Gdi2^{f/f}$ mice,. Scale bar, 10 μm. (E) Quantification of LD diameter from (D), n = 250 LDs pooled from three independent experiments. (F-G) Glycerol (F) and FFA (G) release from sg-NC and *Gdi2*-KO C3H10T1/2 adipocytes stimulated with PBS or CL316243, n = 4 independent experiments. (H-I) Glycerol (H) and FFA (I) release from primary $Gdi2^{AKO}$ and $Gdi2^{f/f}$ adipocytes stimulated with PBS or CL316243, n = 4 independent experiments. (J) Immunoblot analysis of p-CREB, p-HSL, total HSL, and ATGL in sg-NC and *Gdi2*-KO cells after CL316243 stimulation. (K) Immunoblot analysis of GDI2, P62, LC3B, PLIN1, LAMP1, LAMP2, ULK1 in sg-NC and *Gdi2*-KO cells after CL316243 stimulation. (L) Confocal images of LC3B (red) and BODIPY-stained LD (green) in sg-NC and *Gdi2*-KO cells following CL316243 treatment. Arrows denote LC3B puncta associated with LDs. (M) Quantification of LC3B/LD co-localization events per cell. n = 25 cells from three independent experiments. Statistical analysis: C, E-I, two-way ANOVA with Bonferroni's post hoc test; M, one-way ANOVA with Bonferroni's post hoc test. *$P < 0.05$, **$P < 0.01$, ***$P < 0.001$, ****$P < 0.0001$. All data are presented as mean ± s.e.m.

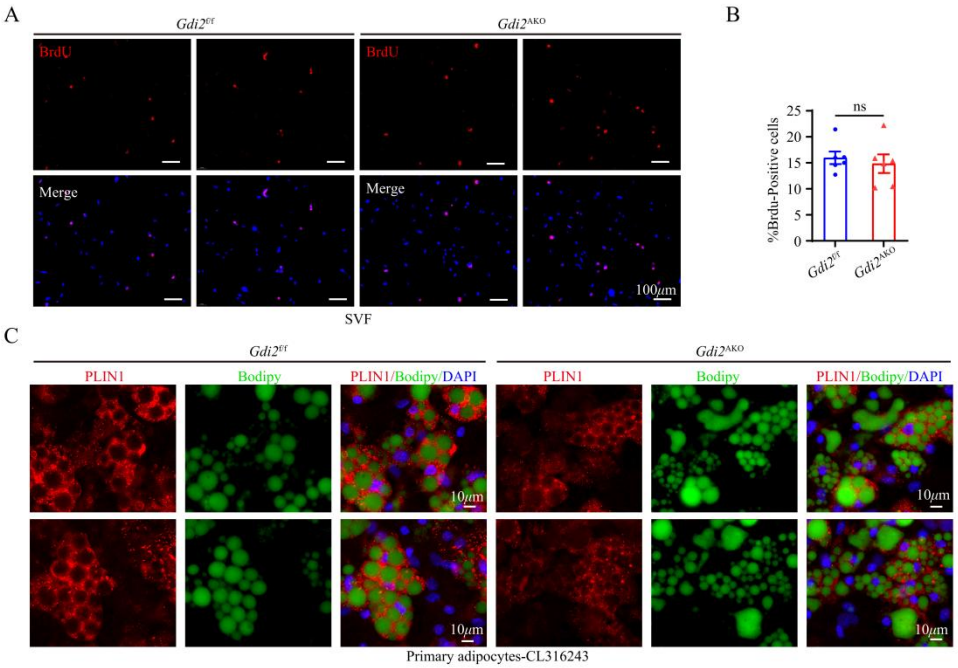


Fig. S5 Proliferation of SVF cells and PLIN1 association with LDs in *Gdi2*-deficient adipocytes.

(A) Representative immunofluorescence images of BrdU incorporation (red) in stromal vascular fraction (SVF) cells isolated from *Gdi2*^{AKO} and *Gdi2*$^{f/f}$ mice. Nuclei were counterstained with DAPI (blue). Scale bar, 100 μm. (B) Quantification of the percentage of BrdU-positive cells in (A). (C) Confocal immunofluorescence images of differentiated primary adipocytes derived from *Gdi2*^{AKO} and *Gdi2*$^{f/f}$ mice, co-stained for PLIN1 (red) and BODIPY (green) after CL316243 stimulation. Nuclei were visualized with DAPI (blue). Scale bar, 10 μm. All data are presented as mean ± s.e.m. Statistical significance in B was determined by unpaired two-tailed Student's *t*-test. ns, not significant.

Adipocyte *Gdi2* deficiency accelerates autophagic flux by promoting late-stage autophagosome-lysosome fusion

Having established that *Gdi2* deficiency enhances lipophagic flux, we next investigated

whether this results from increased autophagosome biogenesis or accelerated late-stage maturation and degradation. Differentiated *Gdi2*-KO and sg-NC C3H10T1/2 adipocytes were stimulated with CL316243 in the presence or absence of 3-methyladenine (3-MA, an early-stage inhibitor of autophagosome formation), chloroquine (CQ, which neutralizes lysosomal pH), or bafilomycin A1 (Baf A1, an inhibitor of vacuolar H^+-ATPase that blocks autophagosome-lysosome fusion). Immunoblot analysis revealed that CL316243-induced reductions in P62, LC3B-II, PLIN1, and PLIN2 were not rescued by 3-MA pretreatment in *Gdi2*-KO cells, indicating that *Gdi2* loss does not enhance autophagosome initiation (Fig. 5A). In contrast, blockade of late-stage autophagy with CQ partially restored LC3B-II, PLIN1, and PLIN2 levels, while Baf A1 treatment completely reversed the CL316243-induced decline of P62, LC3B-II, PLIN1, and PLIN2 in *Gdi2*-KO cells (Fig. 5B-C). Notably, LAMP2 upregulation in *Gdi2*-KO cells persisted under all inhibitor conditions, suggesting that enhanced lysosomal biogenesis or stability occurs independently of autophagic cargo delivery (Fig. 5A-C). Collectively, our findings reveal that *Gdi2* deficiency accelerates the late-stage fusion and degradation, thereby enhancing autophagic flux. To visualize autophagic flux dynamically, we employed a tandem mCherry-EGFP-LC3B reporter. Owing to the pH-sensitive nature of GFP, its fluorescence is rapidly quenched within the acidic lysosomal lumen, whereas mCherry remains stable; thus, yellow puncta ($GFP^+/mCherry^+$) denote non-acidified autophagosomes, while red puncta ($GFP^-/mCherry^+$) represent autolysosomes. CL316243-stimulated *Gdi2*-KO cells exhibited increased red-only puncta and a reduced yellow-to-red ratio (Fig. 5D-F), demonstrating accelerated transition from autophagosomes to autolysosomes.

We further corroborated these findings at the ultrastructural level by transmission electron microscopy (TEM). CL316243-treated *Gdi2*-KO cells displayed a striking accumulation of late-stage autolysosomal compartments, appeared as large, single-membrane vacuoles containing multiple concentric multilamellar bodies, myelin-like figures, and electron-dense lysosomal foci (Fig. 5G-H). Concurrently, mitochondrial abundance was significantly elevated in *Gdi2*-KO cells (Fig. 5I). Moreover, TEM examination of iWAT from cold-exposed *Gdi2*^{AKO} mice revealed markedly smaller LDs, mitochondrial hyperplasia, and abundant autolysosomes, some of which contained recognizable LD remnants, indicating active lipophagy (Fig. 5J-L). Altogether, our results demonstrate that adipocyte *Gdi2* deficiency accelerates autophagic flux by promoting late-stage autophagosome-lysosome fusion, driving the lysosomal degradation of LDs to fuel thermogenesis.

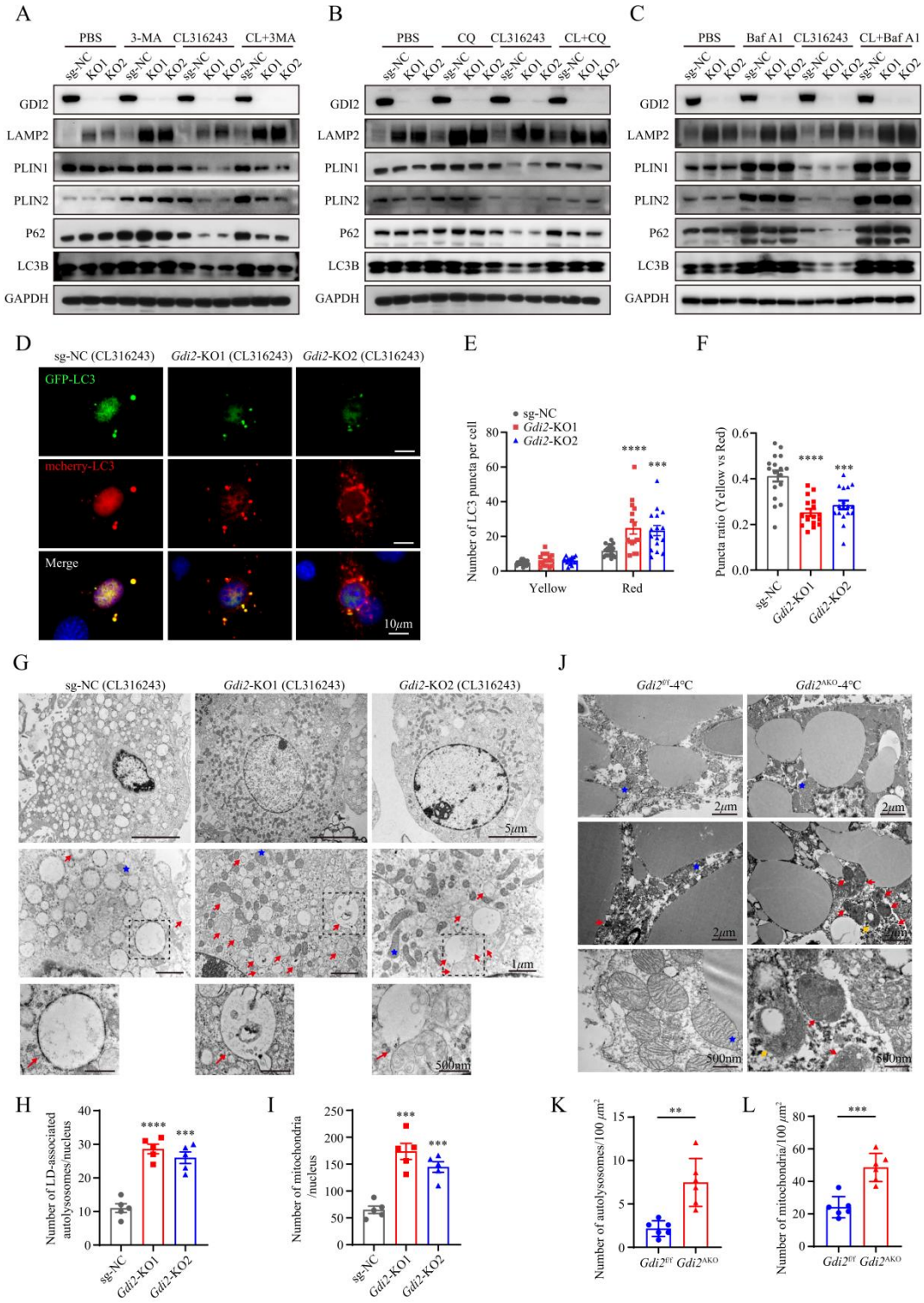


Fig. 5 Adipocyte *Gdi2* deficiency accelerates autophagic flux by promoting late-stage autophagosome-lysosome fusion.

(A-C) Immunoblot analysis of the indicated proteins in sg-NC and *Gdi2*-KO C3H10T1/2 adipocytes treated with CL316243 for 6 h in the presence or absence of 3-MA (5 mM) (A),

CQ (10 μM) (B), or Baf A1 (100 nM) (C). HSP90 served as a loading control. (D) Representative confocal images of sg-NC and *Gdi2*-KO adipocytes expressing the tandem mCherry-EGFP-LC3B reporter after CL316243 stimulation. Yellow puncta ($GFP^+/mCherry^+$) mark autophagosomes; red-only puncta ($GFP^-/mCherry^+$) mark autolysosomes. Scale bar, 10 μm. (E-F) Quantification of yellow and red LC3 puncta per cell (E) and the yellow-to-red puncta ratio (F) from (D), n = 21 cells were analysed from three independent experiment. (G) TEM of sg-NC and *Gdi2*-KO C3H10T1/2 adipocytes after CL316243 treatment. Arrows indicate autolysosomes; blue asterisks mark mitochondria. Insets show enlarged views of the boxed autolysosomes. (H) Quantification of the number of LD-associated autolysosomes per cell from (G). (I)Quantification of mitochondrial number per cell from (G). (J) TEM of iWAT from cold-exposed $Gdi2^{AKO}$ and $Gdi2^{f/f}$ mice. Red arrows indicate autolysosomes; Yellow arrows indicate autolysosomes include LD; blue asterisks mark mitochondria. Note smaller LDs and abundant autolysosomes and mitochondria in $Gdi2^{AKO}$ tissue. (K) Quantification of autolysosome number per 100 μm^2 in iWAT from (J). (L) Quantification of mitochondrial number per 100 μm^2 in iWAT from (J). Data are presented as mean ± s.e.m. Statistical analysis: E, two-way ANOVA with Bonferroni's post hoc test; F,I-J, one-way ANOVA with Bonferroni's post hoc test; K-L, unpaired two-tailed Student's *t*-test. $*P < 0.05$, $**P < 0.01$, $***P < 0.001$, $****P < 0.0001$.

Gdi2 deletion upregulates thermogenic, mitochondrial oxidative phosphorylation, and PPAR signaling gene programs

Given the enhanced lipophagic flux and mitochondrial abundance observed in *Gdi2*-deficient adipose tissue, we next performed RNA-seq of iWAT from cold-challenged

649 *Gdi2*^{AKO} and *Gdi2*$^{f/f}$ mice to profile the transcriptional adaptations. A total of 188 significantly
650 upregulated and 391 downregulated genes were identified in *Gdi2*^{AKO} iWAT relative to
651 controls (Fig. 6A). KEGG pathway enrichment analysis revealed that the upregulated genes
652 were predominantly associated with thermogenesis, oxidative phosphorylation (OXPHOS),
653 and PPAR signaling pathway (Fig. 6B). The heatmap of differentially expressed genes within
654 these three pathways clearly separated *Gdi2*^{AKO} from control samples and revealed
655 upregulation of canonical thermogenic genes such as *Ucp1*, *Dio2*, *Cidea*, *Cox7a1*, *Cox8b*,
656 and *Ucp3*, oxidative phosphorylation components like *Cpt1b*, *mt-Co2*, *Ndufa12*, and *Atp4a,* as
657 well as PPAR signaling-related genes including *Ppara* and *Slc27a2* (Fig. 6C). This
658 coordinated upregulation suggests that *Gdi2* deficiency transcriptionally couples enhanced
659 lipid mobilization with mitochondrial oxidative capacity.

660 To validate the RNA-seq findings, we performed qPCR on iWAT from cold-exposed
661 mice. We first examined a panel of classic thermogenic genes. The mRNA levels
662 of *Ucp1*, *Cidea*, *Dio2*, *Cox7a1*, *Cox8b*, and *Elovl3* were significantly upregulated in
663 *Gdi2*^{AKO} iWAT compared to controls, while *Prdm16* expression remained unchanged (Fig.
664 6D). Next, we assessed the expression of genes associated with mitochondrial OXPHOS. The
665 transcript levels of *Cpt1b*, *Ppargc1a*, and the mitochondrial DNA-encoded
666 genes *mt-Co1*, *mt-Co2*, *mt-Nd2*, and *mt-Nd4*, as well as the nuclear-encoded *Ndufa12*, were
667 all significantly elevated in *Gdi2*^{AKO} iWAT (Fig. 6E). This finding is consistent with the
668 enhanced mitochondrial biogenesis observed by TEM (Fig. 5G-L). Notably, among the PPAR
669 signaling pathway components, *Ppara* and its downstream fatty acid transporter *Slc27a2* were
670 markedly upregulated, whereas *Plin2* and *Acox1* remained unchanged (Fig. 6F). This selective

induction suggests activation of the PPARα transcriptional axis triggered by FFA ligands. In contrast, the expression of general adipocyte differentiation markers (*Pparg*, *Fabp4*, *Glut4*, *Adipoq*, *CD36*, and *Lpl*) did not differ between genotypes (Fig. 6G), indicating selectively activation of thermogenic, OXPHOS, and PPAR pathway genes without altering adipocyte identity. To confirm that this transcriptional reprogramming is adipocyte-autonomous, we utilized differentiated *Gdi2*-KO and sg-NC C3H10T1/2 adipocytes. Upon CL316243 stimulation, the mRNA levels of the PPARα/PGC1α-dependent thermogenic genes *Ucp1*, *Ppargc1a*, and *Cidea* were significantly higher in *Gdi2*-KO cells than in controls (Fig. 6H-J). Consistently, immunoblot analysis revealed that the protein levels of PPARα, PGC1α, and UCP1 were significantly higher in *Gdi2*-KO cells than in controls under CL316243 stimulation (Fig. 6K). Collectively, our results demonstrate that upregulated lipophagy is coupled to a thermogenesis, mitochondrial OXPHOS, and PPAR signaling transcriptional program in *Gdi2*-deficient adipocytes, thereby driving the metabolic remodeling from lipid storage toward energy dissipation.

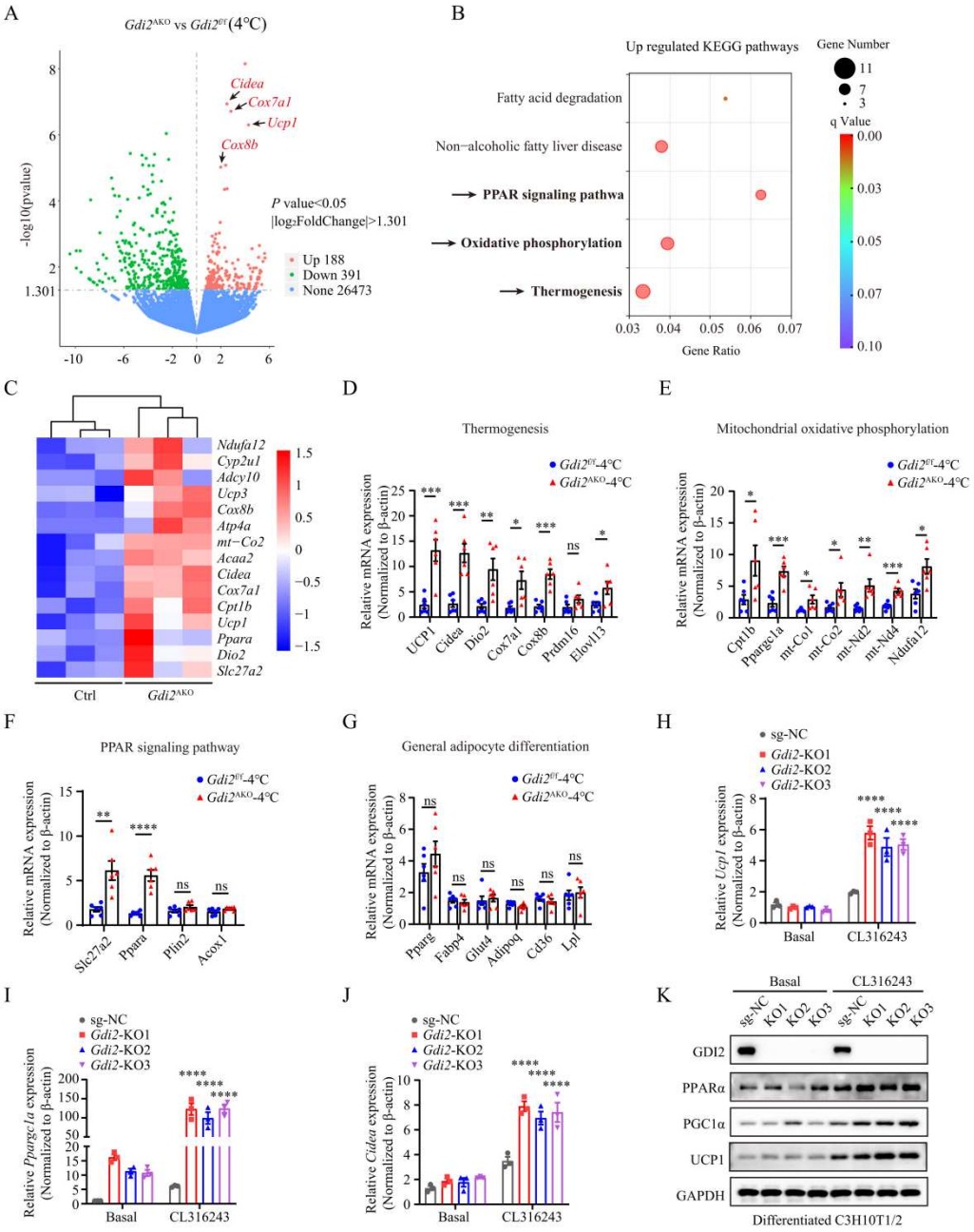


Fig. 6 *Gdi2* deletion upregulates thermogenic, mitochondrial oxidative phosphorylation, and PPAR signaling gene programs.

(A) Volcano plot of differentially expressed genes (DEGs) in iWAT from cold-exposed *Gdi2*^{AKO} and *Gdi2*$^{f/f}$ mice (n = 3 mice per genotype). Red dots, significantly upregulated genes (188); green dots, significantly downregulated genes (391). Significance threshold: $|log_2FC| > 1.301$ and $P < 0.05$. (B) KEGG pathway enrichment analysis of the

upregulated DEGs. The top three enriched pathways are thermogenesis, OXPHOS, and the PPAR signaling pathway. The colour gradient represents $-\log_{10}$(adjusted *P* value), and dot size indicates the number of enriched genes. (C) Heatmap of DEGs associated with the thermogenesis, OXPHOS, and PPAR signaling pathways. Each column represents an individual mouse; each row corresponds to a single gene. The colour scale indicates Z-score-normalized FPKM values. (D) qPCR validation of thermogenic gene expression in iWAT from cold-exposed *Gdi2*^{AKO} and *Gdi2*$^{f/f}$ mice (n = 6 mice per genotype). (E) qPCR validation of mitochondrial OXPHOS-related genes (n = 6 mice per genotype). (F) qPCR validation of PPAR signaling-related genes (n = 6 mice per genotype). (G) qPCR analysis of general adipocyte differentiation markers (n = 6 mice per genotype). (H-J) qPCR analysis of *Ucp1* (H), *Ppargc1a* (I) and *Cidea* (J) in differentiated sg-NC and *Gdi2*-KO C3H10T1/2 adipocytes treated with PBS or CL316243 (n = 3 independent experiments). (K) Immunoblot analysis of PPARα, PGC1α and UCP1 in differentiated sg-NC and *Gdi2*-KO C3H10T1/2 adipocytes under PBS or CL316243 stimulation. HSP90 served as a loading control. All bar graphs are presented as mean ± s.e.m. Statistical comparisons were performed using unpaired two-tailed Student's *t*-test. **P* < 0.05, ***P* < 0.01, ****P* < 0.001, *****P* < 0.0001, n.s., not significant.

Adipocyte *Gdi2* deficiency protects against HFD-induced obesity and metabolic dysfunction

Given that *Gdi2* loss drives lipophagy-dependent lipid mobilization and activates thermogenic and OXPHOS programs, we next asked whether adipocyte *Gdi2* deficiency could confer protection against diet-induced obesity and metabolic dysfunction.

Gdi2^{AKO} and *Gdi2*$^{f/f}$ mice were fed a high-fat diet (HFD) for 16 weeks. Serial monitoring of body weight revealed that *Gdi2*^{AKO} mice started to gain less weight than controls from the seventh week onward (Fig. 7A). Gross morphological examination after 16 weeks showed visibly smaller iWAT, eWAT, and BAT depots in *Gdi2*^{AKO} mice (Fig. 7B-C). In agreement with the leaner phenotype, serum analyses demonstrated lower fasting levels of triglycerides, total cholesterol, and glucose, whereas FFAs were elevated, alongside decreased levels of the hepatic injury marker alanine aminotransferase (ALT) (Fig. 7D). As beige and brown adipocyte function is intimately linked to systemic glucose homeostasis, we next assessed glucose handling and insulin sensitivity. Glucose tolerance tests (GTT) and insulin tolerance tests (ITT) showed that HFD-fed *Gdi2*^{AKO} mice exhibited markedly improved glucose clearance and insulin responsiveness (Fig. 7E-F). HFD-fed *Gdi2*^{AKO} mice exhibited significantly higher O_2 consumption, CO_2 production, and heat generation with unchanged RER and similar food intake, indicating increased total energy expenditure without a shift in substrate utilization (Fig. 7G-I and Supplementary Fig. B-C). H&E staining revealed substantially smaller adipocytes in iWAT, eWAT, and BAT of HFD-fed *Gdi2*^{AKO} mice, consistent with elevated energy expenditure (Fig. 7J). Western blot analysis showed pronounced upregulation of PPARα, PGC1α and UCP1 in iWAT of HFD-fed *Gdi2*^{AKO} mice, supporting a sustained PPARα/PGC1α-driven thermogenic program (Fig. 7K). The obesity-resistant phenotype extended to reduced adipose tissue inflammation, evidenced by diminished F4/80-positive macrophage infiltration in eWAT (Supplementary Fig. 6D). Moreover, HFD-fed *Gdi2*^{AKO} mice exhibited reduced liver weight with alleviated hepatic lipid accumulation (Supplementary Fig. 6E-H). Collectively, our results demonstrate that adipocyte

Gdi2 deficiency maintains a heightened thermogenic program and elevated energy expenditure, protecting against HFD-induced obesity, insulin resistance, glucose intolerance, metabolic inflammation, and hepatic steatosis.

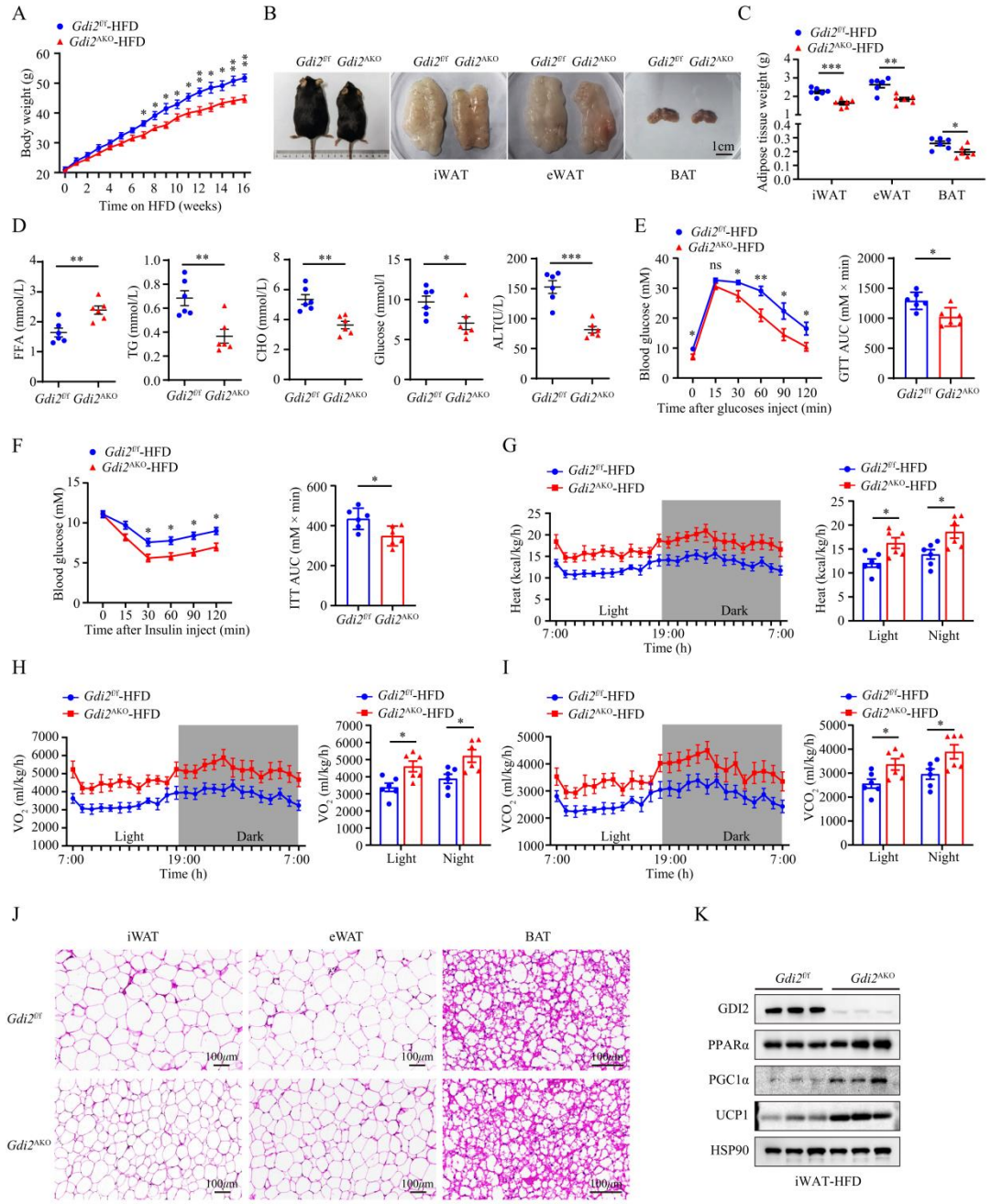


Fig. 7 Adipocyte *Gdi2* deficiency protects against HFD-induced obesity and metabolic dysfunction.

(A) Body weight curves of *Gdi2*^{AKO} and *Gdi2*$^{f/f}$ mice fed a HFD for 16 weeks (n = 6 mice per genotype). (B) Representative gross morphology of mice and their dissected iWAT, eWAT, and BAT depots after 16 weeks of HFD feeding. Scale bar, 1 cm. (C) Quantification of adipose tissue weights normalized to body weight (n = 6 per genotype). (D) Serum levels of fasting FFA, TG, CHO, glucose, and ALT after 16 weeks of HFD (n = 6 per genotype). (E) GTT performed after 16 weeks of HFD. Left, glucose curves; right, area under the curve (AUC) (n = 6 per genotype). (F) ITT after 16 weeks of HFD. Left, glucose curves; right, AUC (n = 6 per genotype). (G-I) Metabolic cage analysis of HFD-fed mice. Hourly profiles of heat production (G), oxygen consumption (VO_2) (H), and carbon dioxide production (VCO_2) (I) over a 24-h period (n = 6 per genotype). (J) Representative H&E staining of iWAT, eWAT, and BAT sections from HFD-fed mice. Scale bar, 100 μm. (K) Immunoblot analysis of PPARα, UCP1 and PGC1α in iWAT lysates from HFD-fed *Gdi2*^{AKO} and *Gdi2*$^{f/f}$ mice. HSP90 served as a loading control. Data are presented as mean ± s.e.m. Statistical analysis: A, E-F (glucose curves), and G-I were analysed by two-way ANOVA with Bonferroni's post hoc test; C-D, and the AUC data in E-F were analysed by unpaired two-tailed Student's *t*-test. *$P < 0.05$, **$P < 0.01$, ***$P < 0.001$, ****$P < 0.0001$.

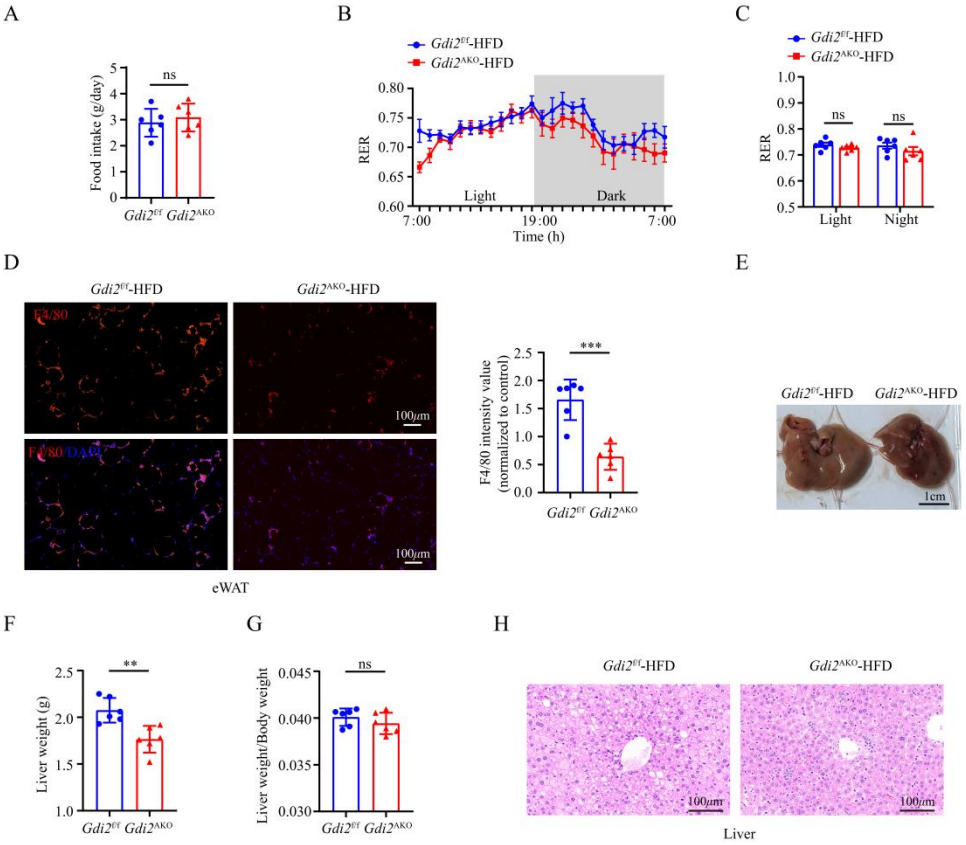


Fig. S6 Metabolic cage assessment, adipose tissue inflammation, and hepatic phenotype in HFD-fed *Gdi2*^{AKO} and control mice.

(A) Daily food intake of *Gdi2*^{AKO} and *Gdi2*$^{f/f}$ mice measured by metabolic cage analysis following 16 weeks of HFD feeding. (B-C) RER recorded during the metabolic cage assessment after 16 weeks of HFD, shown as hourly time-course profiles (B) and average values over the entire recording period (C). n = 6 per genotype. (D) Representative immunofluorescence images of F4/80 in eWAT sections (left) and quantification of F4/80 fluorescence intensity (right), revealing a marked reduction in macrophage infiltration in *Gdi2*^{AKO} mice compared with controls. n = 6 per genotype. Scale bar, 100 μm. (E) Gross morphological images of livers from HFD-fed mice, showing visibly smaller and less steatotic livers in *Gdi2*^{AKO} mice. (F) Liver weight of HFD-fed *Gdi2*^{AKO} and *Gdi2*$^{f/f}$ mice. (G)

Liver weight-to-body weight ratio. (H) H&E staining of liver sections, showing markedly reduced hepatic lipid accumulation in *Gdi2*^{AKO} mice. Scale bar, 100 μm. All data are presented as mean ± s.e.m. Statistical analysis: C, two-way ANOVA with Bonferroni's post hoc test; A, D, F-G, unpaired two-tailed Student's *t*-test. *$P < 0.05$, **$P < 0.01$, ***$P < 0.001$, ****$P < 0.0001$, n.s., not significant.

Discussion

The adaptive thermogenesis of beige adipocytes represents a critical defense against obesity and metabolic dysfunction, a process that depends on the sustained supply of fatty acids to fuel mitochondrial uncoupling and drive thermogenic gene expression [35]. In this study, we identify GDI2 as a novel negative regulator of WAT browning and adaptive thermogenesis., functioning as a molecular brake on lipophagy by preventing late-stage autophagosome-lysosome fusion. Adipocyte *Gdi2* deficiency releases this brake, accelerating the lipophagic degradation of LDs and generating increased FFAs. Increased release of FFAs not only provides substrates for mitochondrial β-oxidation, but also acts as signaling ligands that activate a PPARα-dependent transcriptional program to drive thermogenic and oxidative phosphorylation gene expression. This lipophagy-driven thermogenic reprogramming increases energy expenditure and confers resistance to diet-induced obesity and metabolic dysfunction.

As a member of the GDP dissociation inhibitor family, GDI2 has been implicated in cancer progression, viral infection, and neurodegenerative diseases [36-39]. In the metabolic context, GDI2 participates in adipocyte differentiation and lipid storage [34]. Our data extend the function of GDI2 from static lipid storage into the realm of dynamic energy dissipation. We found that GDI2 expression was positively correlated with BMI in humans and was

upregulated in adipose tissue of obese mice with an inverse relationship to UCP1, and was suppressed by thermogenic stimuli. This dynamic regulation establishes GDI2 as an active participant in adipose tissue metabolic adaptation, capable of translating environmental cues into intracellular trafficking decisions. Its localization at the LD surface, ER-LD contact sites, and autolysosomes further supports a direct role in LD dynamics.

LD catabolism in adipocytes proceeds through canonical neutral lipolysis or lipophagy [16]. Our study identifies GDI2 as a selective suppressor of macrolipophagy independent of neutral lipolysis. Adipocyte *Gdi2* deletion did not alter ATGL/HSL levels or PKA-mediated phosphorylation of HSL and CREB. Instead, *Gdi2*-deficient adipocytes exhibited accelerated autophagic flux upon CL316243 stimulation, including decreased P62 and LC3B-II, PLIN1 degradation, LAMP2 upregulation, and increased LC3B-LD colocalization. Pharmacologic epistasis positioned GDI2 action at the late fusion stage, since Baf A1 and CQ reversed autophagic substrate clearance, whereas 3-methyladenine had no effect. Ultrastructural analysis confirmed the accumulation of degradative autolysosomes, many harboring recognizable LD remnants and multilamellar figures. Together, these data establish GDI2 as a selective suppressor of late-stage macrolipophagy during stimulated LD degradation in adipocytes.

GDI2 is a classical negative regulator of the Rab GTPase family, regulating dynamic membrane trafficking by binding to and sequestering Rab-GDP proteins in a cytosolic inactive pool [32]. A previous study demonstrated GDI2 impairs lipid storage by inhibiting insulin-stimulated Rab18 binding to LD membranes, providing direct experimental evidence that GDI2 can functionally target Rab proteins in adipocytes [34]. We therefore propose a

model in which GDI2 acts as a negative regulator of lipophagic flux by prematurely terminating the GTPase cycle of one or more cognate Rab proteins on the LD surface (Fig. 8). Several Rabs have been functionally implicated at specific steps of lipophagy. At the recognition/initiation step, Rab2 and Rab18 localize on the LD surface and interact with p62 to recruit the autophagic machinery [40]. During the membrane elongation step, Rab10 recruits LC3-positive autophagic membranes and mediates their extension around LDs by forming a complex with EHBP1 and EHD2 [24]. Rab8B participates in autophagosome and autolysosome formation, and its suppression leads to impaired lipophagy and reduced mitochondrial fuel oxidation [41]. At the terminal fusion/degradation step, in which GDI2 functions, Rab7 is the most critical Rab GTPase. In hepatocytes, Rab7 mediates lipophagosome-lysosome fusion under starvation and alcohol exposure [23]. In macrophages from periodontitis patients, aberrant ubiquitination of RAB7A caused by USP4 deficiency impairs autophagosome-lysosome fusion, exacerbating inflammatory progression [42]. Importantly, in adipocytes, Rab7 promotes the recruitment of autophagic components and autophagosome-lysosome fusion upon β3-adrenergic stimulation, contributing to stimulated lipolysis [22]. Additionally, RAB7B suppresses lysosomal degradation of LDs downstream of the TIGAR-LRRK2 axis through both macrolipophagy and chaperone-mediated autophagy (CMA), leading to LD accumulation [43]. The inhibitory role of GDI2 and fusion-promoting function of Rab7 suggests a possible functional antagonism between GDI2 and Rab7 at the LD surface. However, the identity of the specific Rab targeted by GDI2 during stimulated lipophagy remains to be established and represents an important direction for future investigation.

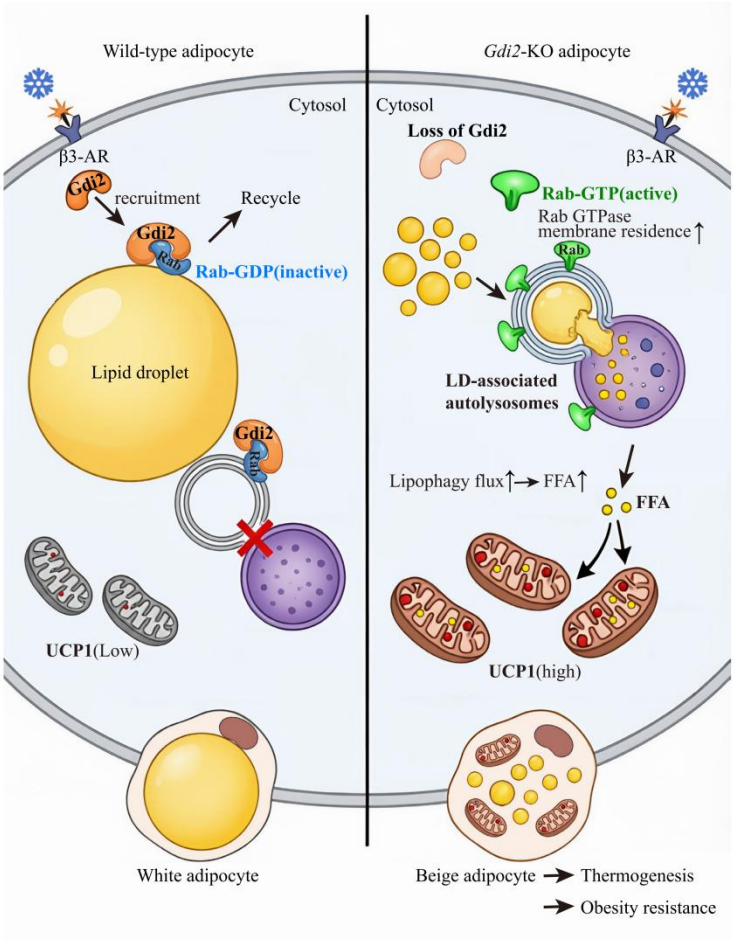


Fig. 8 GDI2 functions as a molecular brake on lipophagy to restrict beige adipocyte thermogenesis.

Schematic model. In both wild-type (left) and *Gdi2*-deficient (right) adipocytes, cold exposure or β3-AR agonists trigger the thermogenic program and stimulate lipolysis. **Left**, in wild-type adipocytes, GDI2 binds to and extracts Rab-GDP from LD-associated membranes, maintaining Rab proteins in a cytosolic inactive state and thereby inhibiting late-stage autophagosome-lysosome fusion. This restricts stimulated lipophagy-dependent LD degradation and limits the supply of FFAs for mitochondrial oxidation and thermogenic gene activation. **Right**, in *Gdi2*-deficient adipocytes, loss of GDI2 increases membrane retention of active Rab-GTP, which promotes autophagosome-lysosome fusion and accelerates

847 lipophagy-dependent LD degradation upon β3-AR stimulation. The resulting elevation in FFA
848 release serves a dual function: FFAs act as substrates for mitochondrial β-oxidation and as
849 signalling ligands that activate a PPARα/PGC1α-dependent transcriptional program. This
850 program upregulates thermogenic genes and oxidative phosphorylation genes, driving
851 mitochondrial biogenesis and uncoupled respiration. The net outcomes are increased energy
852 expenditure, improved glucose homeostasis, and resistance to diet-induced obesity and
853 metabolic dysfunction. The model establishes GDI2 as a key negative regulator that couples
854 stimulated lipophagy to beige fat thermogenesis.

855 RNA-seq of cold-exposed *Gdi2*^{AKO} iWAT identified thermogenesis, oxidative
856 phosphorylation, and PPAR signaling as the top enriched pathways, mechanistically linked to
857 the signaling function of FFAs released by lipophagy. Long-chain FFAs and their derivatives
858 are well-established endogenous ligands for PPARα, a nuclear receptor sensing intracellular
859 lipid levels and transactivating genes governing fatty acid oxidation, mitochondrial biogenesis,
860 and thermogenesis [44-46]. In BAT, PPARα is highly expressed and cooperates with PGC1α
861 upon FFA activation to drive lipid oxidation and thermogenesis [47]. Critically, although
862 PPARα expression is low in WAT, ATGL-mediated lipolysis-derived FFAs can activate
863 PPARα in this depot, promoting mitochondrial activity and WAT browning [48-50].
864 ATGL-deficient mice impaird PPARα activation and mitochondrial respiration, which can be
865 rescued by PPARα agonists [51-53]. Importantly, FFAs generated through the acid lipolysis
866 route are similarly capable of regulating PPARα and its target gene expression [54]. Our data
867 extend this framework by demonstrating that enhanced FFA provision via lipophagy activates
868 the PPARα/PGC1α-dependent thermogenic and OXPHOS program, thereby converting

869 lipid-storing white adipocytes into energy-dissipating beige-like cells. The unchanged
870 expression of general adipogenic markers indicates that *Gdi2* deficiency selectively engages a
871 thermogenic program without perturbing adipocyte identity.

872 Numerous studies demonstrate that enhanced lipid mobilization can improve metabolic
873 health when the released FFAs are efficiently coupled to mitochondrial oxidation. For
874 example, adipose-specific deletion of *Ogt* or *Pak4*, or overexpression of *Cdo1* or *Eepd1*,
875 promotes lipolysis through distinct molecular routes while activating WAT browning,
876 mitochondrial oxidation, and thermogenesis, leading to obesity resistance and improved
877 insulin sensitivity [10, 55-57]. In lipophagy, *FoxO1* channels lipophagy-derived FFAs into
878 AMPK-driven mitochondrial oxidation to maintain energy homeostasis, and adipose-specific
879 *Mtch2* deletion increases energy expenditure and protects against HFD-induced obesity
880 through enhanced autophagic flux [58, 59]. Conversely, elevated circulating FFAs can lead to
881 lipotoxicity. The hyperlipolysis triggered by *Adpla* deficiency produces leanness but results in
882 ectopic lipid deposition and systemic insulin resistance. Here, *Gdi2*^{AKO} mice exhibit elevated
883 energy expenditure, improved glucose tolerance and insulin sensitivity, reduced adipose tissue
884 inflammation, and hepatic steatosis protection. These phenotypes indicate lipophagy-driven
885 FFA release in *Gdi2*-deficient adipocytes is robustly coupled to PPARα/PGC1α-dependent
886 oxidative and thermogenic programs, channeling lipid flux toward metabolic protection rather
887 than lipotoxicity.

888 In summary, this study establishes GDI2 as a molecular brake restricting LD degradation
889 by inhibiting Rab GTPase-dependent late-stage macrolipophagy. Releasing this brake allows
890 enhanced lipophagy to generate FFAs, which act as signaling molecules to activate the

PPARα/PGC1α-dependent transcriptional program, driving mitochondrial biogenesis, uncoupled respiration, and thermogenesis. The functional consequence is comprehensive protection against diet-induced obesity and metabolic dysfunction, positioning GDI2 as a promising therapeutic target for unlocking beige fat thermogenesis to combat obesity and related metabolic disorders.

Data available

The RNA-seq data generated in this study have been deposited in the NCBI GEO under accession code GSE336061. The human adipose tissue RNA-seq dataset reused in this study is available in GEO under accession code GSE162653. Source data are provided with this paper. All other data supporting the findings of this study are included in the article and its supplementary information files, or are available from the corresponding author upon reasonable request.

Conflict of interest

The authors declare that they have no conflicts of interest with the contents of this article.

Author contributions

Fei Gao, Meitian Wang, Sumei Lu, and Guangyong Zhang designed the study; Fei Gao, Yongjiao Zhang, Dong Liu, Yufan Song, Yang Sun, and Meitian Wang performed experiments; Fei Gao, Yongjiao Zhang, and Meitian Wang analyzed data; Fei Gao interpreted results and wrote the manuscript; Fei Gao, Yongjiao Zhang, and Meitian Wang prepared figures; Meitian Wang, Sumei Lu, and Guangyong Zhang reviewed and edited the manuscript; Sumei Lu and Guangyong Zhang supervised the project. All authors approved the final manuscript.

Acknowledgments

This study was supported by grants from the Natural Science Foundation of Shandong Province (ZR2023QH232, ZR2024QH156), the China Postdoctoral Science Foundation (2025M782685) and the Postdoctoral Innovation Project of Shandong Province (SDCX-ZG-202503109).

References

1. Valenzuela PL, P Carrera-Bastos, A Castillo-Garcia, et al., Obesity and the risk of cardiometabolic diseases. Nat Rev Cardiol, 2023. 20(7):475-494.
2. Rubino F, DE Cummings, RH Eckel, et al., Definition and diagnostic criteria of clinical obesity. Lancet Diabetes Endocrinol, 2025. 13(3):221-262.
3. Chew NWS, A Mehta, R Goh, et al., The global cardiovascular-liver-metabolic syndemic: epidemiology, trends and challenges. Nat Rev Cardiol, 2026. 23(4):219-238.
4. Schiborn C, FB Hu, N Stefan, et al., Preclinical and clinical obesity: prevalence, associations to cardiometabolic risk and response to lifestyle intervention in NHANES and the EPIC-Potsdam and TULIP studies. Nat Commun, 2026. 17(1).
5. Cohen P and S Kajimura, The cellular and functional complexity of thermogenic fat. Nat Rev Mol Cell Biol, 2021. 22(6):393-409.
6. Sakers A, MK De Siqueira, P Seale, et al., Adipose-tissue plasticity in health and disease. Cell, 2022. 185(3):419-446.
7. Hagberg CE and KL Spalding, White adipocyte dysfunction and obesity-associated pathologies in humans. Nat Rev Mol Cell Biol, 2024. 25(4):270-289.
8. Shamsi F, CH Wang and YH Tseng, The evolving view of thermogenic adipocytes - ontogeny, niche and function. Nat Rev Endocrinol, 2021. 17(12):726-744.

9. Chen Y, Z Wu, S Huang, et al., Adipocyte IRE1alpha promotes PGC1alpha mRNA decay and restrains adaptive thermogenesis. Nat Metab, 2022. 4(9):1166-1184.
10. Guo YY, BY Li, G Xiao, et al., Cdo1 promotes PPARgamma-mediated adipose tissue lipolysis in male mice. Nat Metab, 2022. 4(10):1352-1368.
11. Jaworski K, M Ahmadian, RE Duncan, et al., AdPLA ablation increases lipolysis and prevents obesity induced by high-fat feeding or leptin deficiency. Nat Med, 2009. 15(2):159-68.
12. Olzmann JA and P Carvalho, Dynamics and functions of lipid droplets. Nat Rev Mol Cell Biol, 2019. 20(3):137-155.
13. Mathiowetz AJ and JA Olzmann, Lipid droplets and cellular lipid flux. Nat Cell Biol, 2024. 26(3):331-345.
14. Henne WM and S Cohen, Heterogeneity, dynamics and organelle interactions of lipid droplets. Nat Rev Mol Cell Biol, 2026.
15. Grabner GF, H Xie, M Schweiger, et al., Lipolysis: cellular mechanisms for lipid mobilization from fat stores. Nat Metab, 2021. 3(11):1445-1465.
16. Zechner R, F Madeo and D Kratky, Cytosolic lipolysis and lipophagy: two sides of the same coin. Nat Rev Mol Cell Biol, 2017. 18(11):671-684.
17. Zhang S, X Peng, S Yang, et al., The regulation, function, and role of lipophagy, a form of selective autophagy, in metabolic disorders. Cell Death Dis, 2022. 13(2):132.
18. Yin G, J Huang, J Petela, et al., Targeting small GTPases: emerging grasps on previously untamable targets, pioneered by KRAS. Signal Transduct Target Ther, 2023. 8(1):212.
19. Ao X, L Zou and Y Wu, Regulation of autophagy by the Rab GTPase network. Cell

Death Differ, 2014. 21(3):348-58.

20. Szatmari Z and M Sass, The autophagic roles of Rab small GTPases and their upstream regulators: a review. Autophagy, 2014. 10(7):1154-66.

21. Haga K and M Fukuda, Comprehensive knockout analysis of the RAB family small GTPases reveals an overlapping role of RAB2 and RAB14 in autophagosome maturation. Autophagy, 2025. 21(1):21-36.

22. Lizaso A, KT Tan and YH Lee, beta-adrenergic receptor-stimulated lipolysis requires the RAB7-mediated autolysosomal lipid degradation. Autophagy, 2013. 9(8):1228-43.

23. Schroeder B, RJ Schulze, SG Weller, et al., The small GTPase Rab7 as a central regulator of hepatocellular lipophagy. Hepatology, 2015. 61(6):1896-907.

24. Li Z, RJ Schulze, SG Weller, et al., A novel Rab10-EHBP1-EHD2 complex essential for the autophagic engulfment of lipid droplets. Sci Adv, 2016. 2(12):e1601470.

25. Kern A and C Behl, On-demand autophagic network adaptations upon limited lipid availability. Autophagy, 2020. 16(7):1348-1350.

26. Li C, X Luo, S Zhao, et al., COPI-TRAPPII activates Rab18 and regulates its lipid droplet association. EMBO J, 2017. 36(4):441-457.

27. Xu D, Y Li, L Wu, et al., Rab18 promotes lipid droplet (LD) growth by tethering the ER to LDs through SNARE and NRZ interactions. J Cell Biol, 2018. 217(3):975-995.

28. Stenmark H, Rab GTPases as coordinators of vesicle traffic. Nat Rev Mol Cell Biol, 2009. 10(8):513-25.

29. Zhen Y and H Stenmark, Cellular functions of Rab GTPases at a glance. J Cell Sci, 2015. 128(17):3171-6.

30. Peng Y, Q Zeng, L Wan, et al., GP73 is a TBC-domain Rab GTPase-activating protein contributing to the pathogenesis of non-alcoholic fatty liver disease without obesity. Nat Commun, 2021. 12(1):7004.
31. Kumar R, M Khan, V Francis, et al., DENND6A links Arl8b to a Rab34/RILP/dynein complex, regulating lysosomal positioning and autophagy. Nat Commun, 2024. 15(1):919.
32. Cherfils J and M Zeghouf, Regulation of small GTPases by GEFs, GAPs, and GDIs. Physiol Rev, 2013. 93(1):269-309.
33. Shisheva A, TC Sudhof and MP Czech, Cloning, characterization, and expression of a novel GDP dissociation inhibitor isoform from skeletal muscle. Mol Cell Biol, 1994. 14(5):3459-68.
34. Guzman-Ruiz R, C Tercero-Alcazar, Y Rabanal-Ruiz, et al., Adipose tissue depot-specific intracellular and extracellular cues contributing to insulin resistance in obese individuals. FASEB J, 2020. 34(6):7520-7539.
35. Yin X, Y Chen, R Ruze, et al., The evolving view of thermogenic fat and its implications in cancer and metabolic diseases. Signal Transduct Target Ther, 2022. 7(1):324.
36. Maldonado H, M Dreger, LD Bedgood, et al., A trafficking regulatory subnetwork governs alpha(V)beta(6) integrin-HER2 cross-talk to control breast cancer invasion and drug resistance. Sci Adv, 2024. 10(49):eadk9944.
37. Sun Y, H Zheng, L Qian, et al., Targeting GDP-Dissociation Inhibitor Beta (GDI2) with a Benzo[a]quinolizidine Library to Induce Paraptosis for Cancer Therapy. JACS Au, 2023. 3(10):2749-2762.

38. Wang M, X He, J Li, et al., GDI2 deletion alleviates neurodegeneration and memory loss in the 5xFAD mice model of Alzheimer's disease. Biochim Biophys Acta Mol Basis Dis, 2024. 1870(4):167093.
39. Yin S, Y Tao, T Li, et al., Itaconate facilitates viral infection via alkylating GDI2 and retaining Rab GTPase on the membrane. Signal Transduct Target Ther, 2024. 9(1):371.
40. Zhao P, R Tian, D Song, et al., Rab GTPases are evolutionarily conserved signals mediating selective autophagy. J Cell Biol, 2025. 224(5).
41. Kim YS, HJ Nam, CY Han, et al., Liver X Receptor Alpha Activation Inhibits Autophagy and Lipophagy in Hepatocytes by Dysregulating Autophagy-Related 4B Cysteine Peptidase and Rab-8B, Reducing Mitochondrial Fuel Oxidation. Hepatology, 2021. 73(4):1307-1326.
42. Kang S, S Liu, X Dong, et al., USP4 depletion-driven RAB7A ubiquitylation impairs autophagosome-lysosome fusion and aggravates periodontitis. Autophagy, 2025. 21(4):771-788.
43. Zhang T, KG Linghu, J Tan, et al., TIGAR exacerbates obesity by triggering LRRK2-mediated defects in macroautophagy and chaperone-mediated autophagy in adipocytes. Autophagy, 2024. 20(8):1741-1761.
44. Bougarne N, B Weyers, SJ Desmet, et al., Molecular Actions of PPARalpha in Lipid Metabolism and Inflammation. Endocr Rev, 2018. 39(5):760-802.
45. Montaigne D, L Butruille and B Staels, PPAR control of metabolism and cardiovascular functions. Nat Rev Cardiol, 2021. 18(12):809-823.
46. Sluse FE, W Jarmuszkiewicz, R Navet, et al., Mitochondrial UCPs: new insights into

regulation and impact. Biochim Biophys Acta, 2006. 1757(5-6):480-5.

47. Barbera MJ, A Schluter, N Pedraza, et al., Peroxisome proliferator-activated receptor alpha activates transcription of the brown fat uncoupling protein-1 gene. A link between regulation of the thermogenic and lipid oxidation pathways in the brown fat cell. J Biol Chem, 2001. 276(2):1486-93.

48. Gross B, M Pawlak, P Lefebvre, et al., PPARs in obesity-induced T2DM, dyslipidaemia and NAFLD. Nat Rev Endocrinol, 2017. 13(1):36-49.

49. Rachid TL, A Penna-de-Carvalho, I Bringhenti, et al., Fenofibrate (PPARalpha agonist) induces beige cell formation in subcutaneous white adipose tissue from diet-induced male obese mice. Mol Cell Endocrinol, 2015. 402:86-94.

50. Zhou L, M Yu, M Arshad, et al., Coordination Among Lipid Droplets, Peroxisomes, and Mitochondria Regulates Energy Expenditure Through the CIDE-ATGL-PPARalpha Pathway in Adipocytes. Diabetes, 2018. 67(10):1935-1948.

51. Ahmadian M, MJ Abbott, T Tang, et al., Desnutrin/ATGL is regulated by AMPK and is required for a brown adipose phenotype. Cell Metab, 2011. 13(6):739-48.

52. Haemmerle G, T Moustafa, G Woelkart, et al., ATGL-mediated fat catabolism regulates cardiac mitochondrial function via PPAR-alpha and PGC-1. Nat Med, 2011. 17(9):1076-85.

53. Schoiswohl G, M Stefanovic-Racic, MN Menke, et al., Impact of Reduced ATGL-Mediated Adipocyte Lipolysis on Obesity-Associated Insulin Resistance and Inflammation in Male Mice. Endocrinology, 2015. 156(10):3610-24.

54. Radovic B, N Vujic, C Leopold, et al., Lysosomal acid lipase regulates VLDL synthesis

and insulin sensitivity in mice. Diabetologia, 2016. 59(8):1743-52.

55. Chen S, Y Wang, Q Zhou, et al., Myristoylated Eepd1 Enhances Lipolysis and Thermogenesis through PKA Activation to Combat Obesity. Nat Commun, 2025. 16(1):651.

56. Yang Y, M Fu, MD Li, et al., O-GlcNAc transferase inhibits visceral fat lipolysis and promotes diet-induced obesity. Nat Commun, 2020. 11(1):181.

57. Yu HC, YG Jeon, AY Na, et al., p21-activated kinase 4 counteracts PKA-dependent lipolysis by phosphorylating FABP4 and HSL. Nat Metab, 2024. 6(1):94-112.

58. Lettieri Barbato D, G Tatulli, K Aquilano, et al., FoxO1 controls lysosomal acid lipase in adipocytes: implication of lipophagy during nutrient restriction and metformin treatment. Cell Death Dis, 2013. 4(10):e861.

59. Zhao XY, BC Zhao, HL Li, et al., MTCH2 Suppresses Thermogenesis by Regulating Autophagy in Adipose Tissue. Adv Sci (Weinh), 2025. 12(17):e2416598.

Supplementary Files

This is a list of supplementary files associated with this preprint. Click to download.

- SupplementaryData.docx